Alkali-containing molecular ions in Secondary Ion Mass Spectrometry (SIMS): An innovative technique for chemical analysis of quantum structures

Purushottam Chakraborty

Saha Institute of Nuclear Physics, Kolkata 700 064, India

ARTICLE INFO

ABSTRACT

Continuous progress in the understanding of fundamental and instrumental aspects of Secondary Ion Mass Spectrometry (SIMS) has made this technique extremely powerful for the analysis of materials. Secondary ion-emission is a complex phenomenon and amongst various mechanisms, the 'electron-tunnelling model' based on the survival probability of an escaping ion above the surface is the widely accepted notion in the understanding of ionization probability for positive and negative ions. As the secondary-ion intensity of a particular element strongly depends on the ionization efficiency of a sputtered atom or molecule, instantaneous local chemistry of the sample surface plays a significant role in the secondary-ion emission. This is the so-called "Matrix Effect", which makes the SIMS technique challenging for quantification in spite of its highest detection sensitivity (<ppb) and exceptional depth-resolution (<1 nm). Therefore, the compensation of "matrix effect" is required. If alkali-metals such as Li, Rb, K, Na, Cs, ...etc. (referred to as 'A') are present in the neighbourhood of the probing element (M) on a sample-surface, a quasi-molecular $(MA)^+$ ion can be formed by the attachment of this alkali-ion with a sputtered atom (M^0) in the close proximity of sample surface. Such phenomenon can occur if an alkali-ion beam is chosen as the impinging ion-beam for sputtering. The $(MA)^+$ molecular-ions that are formed in the SIMS process have strong correlation with the atomic polarizability of the element M. As the emission process for M^0 is decoupled from the MA^+ ion formation process, the 'matrix effect' drastically decreases. This is very similar to the ion formation in "secondary neutral mass spectrometry" (SNMS). Although the detection of $(MA)^+$ molecular ions has found its applicability in materials quantification without calibration standards, it generally suffers from a low useful yield. In such case, the detection of $(MA)_2^+$ molecular-ions offers a better sensitivity (by orders of magnitude), as the yields of $(MA)_2^+$ molecular-ions have been found to be much higher compared to that of $(MA)^+$ molecular-ions. Monitoring of molecular-ions is often employed in standard SIMS experiments to improve the detection of sputtered ion-species which show poor dynamic ranges or are affected by mass interference. For example, while making SIMS analysis of GaAs, carbon as an impurity-element is detected by monitoring $(AsC)^+$ molecular-ions instead of C^- ions, because the latter has a high background arising from residual-gas species in the analysis chamber. Cs is highly preferred for MCs^+ or MCs_2^+ molecular-ions in SIMS because of the strongest reactivity and electropositive nature of caesium. The present chapter deals with an in-depth discussion on the ion-emission phenomena in sputtering, 'matrix effect' and its compensation, and the potential application of MCs_n^+ - based SIMS method for quantitative chemical analysis of materials. A special prominence has been given on the quantification of low-dimensional materials, superlattices and quantum structures using this innovative "MCs_n^+ -SIMS" (n = 1, 2, ...) approach in all complexities.

1. Introduction

The rapidly growing importance of advanced materials research stems from the ever-increasing importance of low-dimensional structures. For example, some fast developing areas are: thin film structures for microelectronics with tailored electrical properties, optical films and coatings with specific anti-reflecting properties, ion-beam modified surfaces with high resistance to wear and corrosion, etc. Controlled fabrication of these materials requires a detailed and reliable, spatially-resolved chemical and structural analysis. In view of their planar structures, the analysis of in-depth distributions of chemical composition with high resolution is of primary importance, particularly at near-surfaces

*Corresponding author: E-mail address: purushottam.chakraborty@gmail.com (P. Chakraborty).

and interfaces. For this purpose, numerous methods have been developed during past few decades. Among these, micro-sectioning techniques based on sputtering in combination with surface analytical methods are most frequently used because of their wide-ranging applicability to practically any kind of materials. These methods allow the realization of optimum depth resolution (down to a few atomic monolayers) over a wide depth-range up to several microns facilitating the quantitative analysis of interfaces of thin films, superlattices and quantum structures. The sputtering process itself, however, is independent of the analysis method and should therefore be considered as a separate physical process. Sputtering can be accomplished by removing atoms from the top monolayers of a solid. Therefore, a depth-resolution in the monolayer regime should in principle be achievable. However, sputtering does not occur by an ideal layer-by-layer removal but is the result of a complex ion–surface interaction process. This process introduces a variety of distortional effects into the original morphology and composition of a sample, which are the cause of the much more extended profile broadening that is generally observed. Fig. 1 represents a general experimental arrangement for surface analysis.

In the context of sputter-depth profiling, Secondary Ion Mass Spectrometry (SIMS) has exclusively placed its importance amongst other methods of surface and interface analysis. SIMS is essentially a sputtering phenomenon in which the transfer of momentum from the energetic impinging primary ions to the sample surface causes the ejection of surface-atoms and -molecules. A tiny fraction of the sputtered particles is ionized, positive and negative; which are termed as 'secondary-ions'. In the sputtering process, the bombarding ion transfers energy in

collisions to target atoms, which recoil with sufficient energy to generate other collisions. Some of the backward recoils in the generated 'collision cascade' approaches the surface with enough energy so as to overcome the surface binding energy and eventually to escape from the solid. Therefore, the secondary sputtered species originate from the collision cascades that are created within the target lattice and from recoil sputtering. In the linear cascade regime, the sputtering yield is proportional to the number of recoil-atoms that is proportional to the energy deposited per unit depth in nuclear processes (particle velocity much less than the Bohr velocity). Effective thickness of the sputtered layer arising out of a single collision cascade is of the order of an atomic dimension and its estimate can be obtained from a simple expression of the sputtering-yield involving information depth, typical average energy of the sputtered particles and nuclear stopping power [1]. As the ejected particles originate essentially from the outermost (~1-3) atomic layers, they carry information about the composition of the surface and near-surface region. The varieties of the sputter-products constitute electrons, atoms, atomic clusters, molecules 'intact' and distinctive molecular fragments. A very small fraction of the sputtered atoms or molecules may be excited above their respective ground-states. The atoms (or ions) sputtered in the excited states may subsequently go through two processes.

1. Radiative electronic transition via de-excitation of the excited neutral (or ionic) species leading to the emission of photons in the range ultra-violet to visible optics.

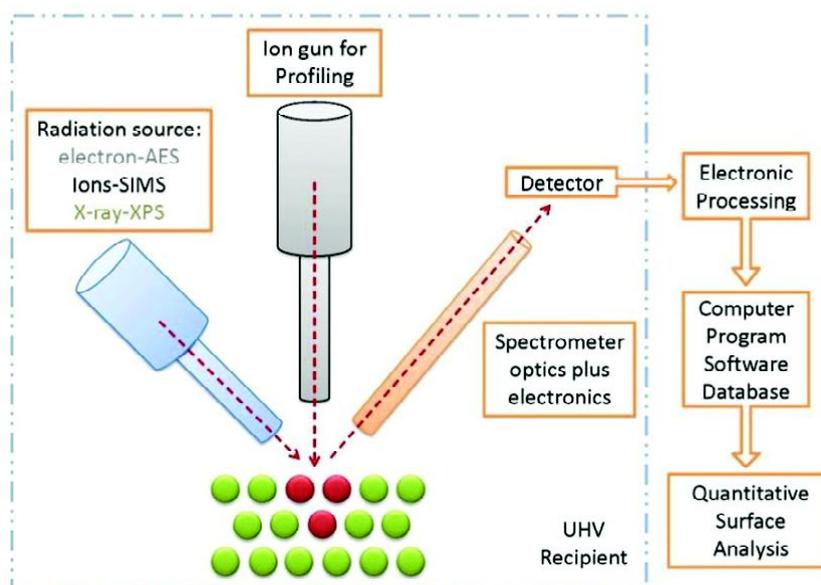2. Non-radiative electronic transition leading to the emission of Auger electrons or to the ionization of the

Fig. 1. Schematic diagram of the principal arrangement of a standard surface analytical instrument.

sputtered species via resonant-tunnelling of electrons from these species to the valence band of the solid.

The above dynamic charge-transfer processes occurring between the escaping sputtered atom and the solid surface are further complicated by the strong electronic and structural perturbations from the ion bombardment.

Secondary emission of ions (as well as photons) in the sputtering process is an inelastic phenomenon in ion-surface interactions and has tremendous important applications in materials analysis. A secondary ion mass spectrum consists of almost all elements present on the top surface in elemental or compound form. These secondary ions have large kinetic energy distributions mostly peaked at around 2-5 eV. The energy-selected ionized fraction of the sputtered species is mass analysed and detected using a combination of a suitable mass spectrometer and an appropriate ion-collection optics, thus allowing to get a variety of information about the surface, subsurface, or bulk composition of the sample. As the ion-bombardment goes on, the material is continuously eroded atomic layer by atomic layer, thus providing the in-depth quantitative information about the material constituents through dynamic SIMS. Although this mode of SIMS is essentially a destructive process (that is, the sample is irreversibly consumed in the course of analysis); this problem is largely ameliorated by the highest detection sensitivity of this technique, allowing the required information to be obtained from tiny volumes of materials.

As the secondary-ion intensity of a particular element strongly depends on the ionization efficiency of a sputtered atom or molecule of that element, instantaneous local surface chemistry of the sample plays a significant role in the secondary ion emission in the SIMS process. For example, the presence of some electronegative element like oxygen or some electropositive element like caesium on the top surface of a host matrix increases the emission of secondary positive or negative ions, respectively by several orders of magnitude. Such ion-yield variation of a particular element in a matrix of instantaneously varying surface chemistry is the so-called matrix effect in SIMS, resulting in a non-linear dependence of secondary ion-signals on the concentration of that element in the matrix. Although this 'matrix effect' is an artefact of the SIMS technique, this is often consciously desired in analysing the elements of extremely low ion-yields. Obviously, the matrix effect requires to be appropriately compensated or corrected while estimating the actual concentration of a certain species present in the host ('matrix'). The compensation is usually done either by using some "calibration standards" or through "relative sensitivity factor" (RSF) approach. However, the strong dependence of the ionization

probability on the substrate properties places remarkably strict constraints on the use of acceptable standards in making quantitative analysis through SIMS. In this context, the use of 'ion-implanted standards' has reached a high level of sophistication, allowing precision measurements in SIMS quantification [2]. From an analytical point of view, motivation towards the reduction of the matrix effect has led to the development of another technique called "secondary neutral mass spectrometry" (SNMS). Non-dependence of the secondary neutral-yield on the local surface chemistry makes this technique quantitative straight way without the need of calibration standards [3]. Besides, SNMS has the potential to measure depth profiles without preferential sputtering artifacts, as opposed to electron spectroscopic techniques. Although SNMS has detection limits and dynamic range much worse than that of SIMS, it has proved to be somewhat established for routine thin film analysis.

A great success in the complete suppression of matrix effect has been achieved using "alkali-ion based molecular SIMS" approach [4]. If alkali elements such as Li, Rb, K, Na, Cs, …etc. (referred to as A in general) are present in the neighbourhood of the probing element (M) on a sample surface, quasi-molecular ions can be formed by the attachment of these alkali ions [$(MA)^+$ formation] in theSIMS process. The formation of these $(MA)^+$ molecular-ions has strong correlation with the atomic polarizability of the element M. The emission process for the re-sputtered species M^0 is decoupled from the MA^+ ion formation process, in analogy with the ion formation in SNMS, resulting in a drastic decrease in the conventional 'matrix effect' in SIMS. Although the detection of MA^+ molecular ions in SIMS has found its applicability in direct materials quantification, it generally suffers from a low useful yield. In such case, detection of $(MA)_n^+$ [n = 2, 3……] molecular-ions offers better sensitivity (even by several orders of magnitude), as the yields of such molecular-ion complexes have often been found to be much higher than that of MA^+ ions. The recombination coefficient of MA^+ or MA_2^+ molecular species depends on the electro-positivity or electro-negativity of the element M, respectively. Apart from the surface binding energy of the respective uppermost monolayer, the changes in 'local surface work-function' have often been found to play a significant role in the emission of these molecular ions.

The SIMS technique, owing to its exceptionally high detection sensitivity, is extremely powerful to quantify an ultra-trace element present in a matrix with its concentration below parts per billion. The elemental detection sensitivities in dynamic SIMS (primary-ion current density ~$\mu A/cm^2$) are much higher (by few orders of magnitude) compared to that in static SIMS (primary-ion current density ~pA/cm^2), as the ion detection sensitivity in dynamic SIMS scales with the analytical volume consumed in SIMS depth

profiling [5]. The major scientific (and also economic) impact of dynamic SIMS is the in-depth analysis of semiconductor materials, where low levels of dopants are analysed in successive thin slices of materials ~ 5 nm thick. The flexibility of sputter-sectioning, in combination with the major advantages of the superior mass spectrometric techniques, such as large dynamic ranges both in the mass separation and detection systems, has enabled the dynamic SIMS to be extremely sensitive for the analysis of solid surfaces, thin films, multilayers, superlattices and even low-dimensional structures. However, If the aim of the measurement is to obtain compositional information of the top most surface of a material with its minimal damage, the main problem is to ensure that sufficient signal is obtained at the desired spatial resolution whilst minimizing the ion flux incident on any part of the surface. This is easily achieved by switching from the traditional instrumental approach of using continuous-flux ion guns and quadrupole or sector-magnetic field mass spectrometer to a combination of pulsed-ion sources with time-of-flight (TOF) mass spectrometers. The TOF-SIMS is a much more efficient way of acquiring spectral data, and also provides considerably good resolution and sensitivity up to very high masses. Using such instruments, SIMS images with a spatial resolution of better than 10 nm are obtainable. TOF-SIMS is a widely used technique for depth profiling applications in many areas, and has progressively expanded from microelectronics to materials science to biology [6]. The present chapter has addressed the fundamentals, general perspectives of SIMS and the phenomenal challenges of "alkali-based molecular-ion SIMS" in 'materials quantification without calibration-standards', explicitly high lighting the conceptual understanding of the formation mechanisms of MA_n^+ (n = 1, 2, ...) molecular-ion complexes. Fig. 2 represents the schematic layout of the SIMS process and an experimental arrangement, respectively.
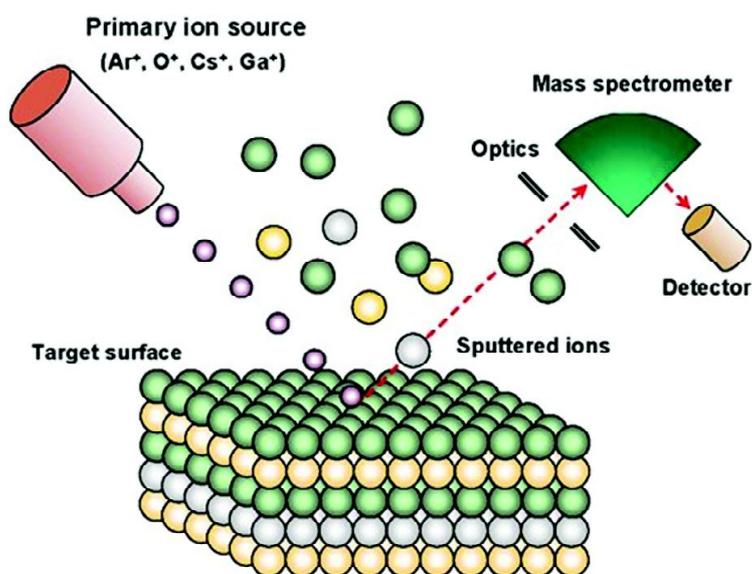

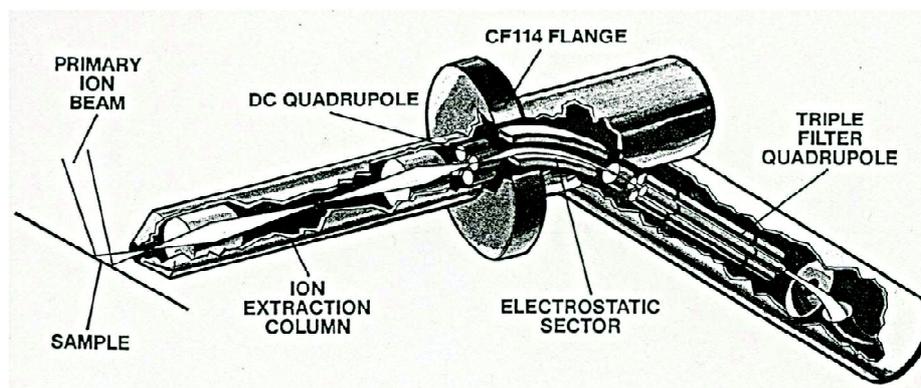**Fig. 2a.** Schematic representation of SIMS [2].

Fig. 2b. Schematic layout of a SIMS setup (HAL EQS1000). It employs a triple-quadrupole filter and a 45^0 sector-field electrostatic energy-analyzer with DC quadrupole input focusing lens [2].

2. Secondary ion emission phenomena

Simplistically, the important parameters are the ionization potential (I) and the electron affinity (A) for positive ionization and negative ionization, respectively. For a metallic target, the relevant energy parameter is the work function (ϕ). The quantity (I-ϕ) is the minimum amount of energy required to ionize positively an atom at infinity and deposit the electron on the solid surface; a situation analogous to the sputtering of a positive ion. Similarly, (ϕ-A) is the amount of energy required to transfer an electron from the solid surface to an atom at infinity to form a negative ion. Hence the formation probability of a secondary ion, either positive or negative, has a functional dependence on these three quantities. The surface work function ϕ is affected by the modification in the surface chemistry causing thereby significant changes in the secondary ionization probabilities. Although there is no consensus concerning a universal ion emission model, a simple picture is believed to hold for the major part of the sputtered ion-flux (n^+ and n^-) that scales approximately as:

$$n^+ = B \exp (\phi\text{-}I)/K$$

$$n^- = B' \exp (A\text{-}\phi)/K'$$

where B, B', K, K' are suitable constants. Andersen and Hinthorne [7] gave the first convincing demonstration of such scaling, while comparing the ionization probabilities for several elements sputtered from a common matrix. They were the first to compare the intensities of the positive ion signals for species sputtered from a single matrix and found a linearity of the plots with the ionization potentials of the sputtered species restricted to elements with ionization potentials in the range 5–10 eV. From the similarity of the data to those which could be theoretically obtained from high-temperature plasma in thermal equilibrium with relative ion populations governed by an equation of the form

$$\frac{n^+}{n^0} \propto \exp\left(\frac{-I}{kT}\right) \tag{1}$$

it was proposed that the sputtering-site physically resembles a plasma in the state of local thermodynamic equilibrium (LTE). The ions, electrons and neutral atoms in the plasma exist in thermal equilibrium and their energy-distributions are governed by the Boltzmann distribution of velocities. Here k is the Boltzmann constant and T is the plasma temperature, respectively. Expression (1) essentially gives the secondary ion emission cross-section for positive ions considering the applicability of LTE model. Andersen and Hinthorne [7] applied the concept of LTE using the Saha-Langmuir equation for thermal ionization and included the electron density term, n_e, for the calculation of the dissociation constant of the form

$$\frac{n^+ n_e}{n^0} = \frac{u^+(T)}{u^0(T)} 2 \frac{(2\pi m k T)^{3/2}}{h^3} e^{\frac{-(E-\Delta E)}{kT}} \tag{2}$$

where n^+, n^0 and n_e are the density of positive ions, neutral atoms and electrons, respectively, in the plasma. Here, u^+, u^0 and 2 are the partition functions of the ions, atoms and electrons, respectively, in the plasma. I and ΔI are the ionization potential of the element and its reduction in the plasma, respectively. T is a parameter equivalent to "temperature". The term (kT) with dimension of energy reflects the average energy of an atom in the collision cascade.

The expression for the positive ionization probability $\beta^+(= n^+/n^0)$, as derived from equations (1) and (2), is thus

$$\beta^+ \propto n_e^{-1} \exp\left(\frac{-I}{kT}\right) \tag{3}$$

Eq. (3) explains why the positive ionization probability increases for oxides, thus explaining the matrix effect. The increase of electronic work function in a surface with the presence of oxygen or in an oxide surface causes a decrease in the electron density n_e in the local plasma, thereby decreasing the probability of neutralization of the emitted positive ions. Similarly, the decrease of work function for caesium-coated surface causes an increase of n_e giving rise to a decrease in the positive ion emission or increase in the negative ion emission. Therefore, the LTE model explains the matrix effect quite effectively. However, since this model stems essentially from thermodynamic arguments it does not predict the strong yield-dependence on ion emission velocity. Furthermore, the model formidably fails to explain the varying nature of kinetic energy distributions of sputtered atomic-, molecular- and cluster-ion species, in contrast to the Boltzmann distributions.

Another approach is based on the "bond-breaking concept" [8] to explain the matrix effect observed during the sputtering of ionic solids. Later, it was proposed [9] that it should also be appropriate for compounds like oxides, where the bonds formed have only a partial ionic character. In this concept, the ionization of a sputtered metal atom, during the breaking of the chemical bond with an electronegative atom on the surface, is qualitatively similar to the Landau-Zener treatment of ion-pair dissociation of polar molecules [10]. Based on this concept, Yu and Mann [11] have described the enhanced positive metal-ion emission from metal oxides. The sputtering of the metal atom M through breaking of the oxide-bond creates an oxygen-surrounded cation vacancy X at the surface. This oxygen-surrounded vacancy, with an electron affinity A, strongly attracts an electron at the expense of the ejected particle M, causing the positive secondary ion-yield enhancement. Analogous arguments hold for the effect of

Cs on negative ion emission. For few tens of eV, the positive ionization probability β^+ approximately follows a power-law dependence on on ion energy. The model however, was found to be restricted to the emission of positively-charged ions, whereas its applicability to negative secondary ions, molecular-ions and multiply-charged ions has not been established.

The electron-tunnelling model [12,13] on the other hand describes the ionization probability for both positive and negative ions, based on the survival probability of an escaping ion above the surface. Fig. 3 shows schematically the electron-tunnelling phenomenon [2]. Conceptually, it is a model framed on the basis of the crossing of the discrete electronic level of the sputtered ion with many electronic levels (continuum states) of the solid. The central feature of this continuum of electronic states is the Fermi level that separates the occupied and unoccupied states. The position of the Fermi level plays an important role in the survival probability of the escaping ion above the surface [2]. The variations in the image potential and the chemical force of the system cause E_a to vary with the separation z between the atom and the surface. For $E_a = E_F$ at the crossing point, electrons in the metal can tunnel out to fill in the atomic level. This allows resonant electron-tunnelling between the outgoing ion and the target surface, leading to neutralization of the positive ion. If $E_a(z)$ varies rapidly with z and crosses E_F at the crossing distance z_c from the surface with a large slope, the survival probability (P) of an ion has an exponential dependence on both $\Delta(z_c)$ and $v_\perp$:

$$P \cong \exp\left[-\frac{2\Delta(Z_c)}{\hbar\gamma v_\perp} \right] \quad (4)$$

where $\Delta(z_c)$ and $v_\perp$ are atomic level-width at the crossing point and the normal component of the ion-emission velocity, respectively. The exact functional dependence of P on ion-emission velocity v varies according to the way E_a and $\Delta(z)$ change with z. For a small change of surface work-function ϕ, expressions for the positive and negative ionization probabilities are respectively expressed [2] as:

$$\beta^+ \propto \exp\left[-\frac{(I - \phi)}{v_\perp} \right] \quad (5)$$

$$\beta^- \propto \exp\left[-\frac{(\phi - A)}{v_\perp} \right] \quad (6)$$

where **I** and **A** are ionization probability and electron affinity of the sputtered species, respectively. Eqs. (5) and (6) clearly exhibit the importance of the position of the Fermi level in the ionization probabilities. The electron-tunnelling model has reasonably explained the observed dependence of the ionization probabilities on work-function, emission-velocity and emission-angle for the atoms sputtered from layers adsorbed on metallic surfaces.
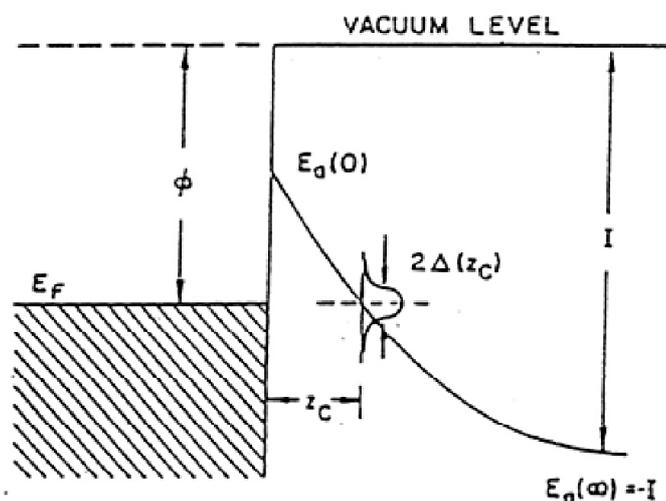

Fig. 3. Schematic energy diagram of a sputtered ion leaving a metal surface. The Fermi level ε_F lies below the vacuum level by the work function φ. The energy level of the sputtered ion (ε_a) is a function of the distance z from the surface. At a distance far from the surface ε_a is the ionization potential I of the element. $\varepsilon_a = \varepsilon_F$ at the crossing point (z_c). Here the width $2\Delta(z)$ of ε_a is a measure of the electron tunneling probability [2].

3. Quantification

3.1. "Matrix Effect" in SIMS

Irrespective of the mechanism of secondary ion formation, quantification in dynamic SIMS is universally accepted as the conversion of a secondary ion-current I(t) of a given species in a homogeneous target matrix, measured as a function of time t, to a concentration C(z), measured as a function of depth z. Calibration of the depth scale is based on a strictly linear proportionality between the elapsed erosion-time and the eroded depth of the sample, considering unaltered sputtering conditions throughout the measurement and consequently a fixed erosion rate. In reality, however, the linear time-to-depth mapping may not be strictly valid as the erosion by ion-bombardment introduces smearing of depth information by both target atom relocation and by surface topography development. Provided there exists a stationary situation between a surface matrix composition and the impinging ion beam, the secondary ion current of a species (x) in a target matrix (m) can be expressed by the relation [2] as

$$I_x^\pm = I_p Y_{tot}\, \beta^\pm_{x,\,m} f(\Delta E)\, f(\Delta\Omega)\, T_{x,m}\, \eta_{x,m} C_x \quad (7)$$

where $I_x^\pm$ (positive or negative) is the isotope-corrected secondary ion current (i.e. $I_x^\pm = I_{xi}^\pm/x_i$, $I_{xi}^\pm$ is the measured ion current of

isotope i of element x, and x_i is its isotopic abundance). I_p is the primary ion current (= $j_p.S$, where j_p is the primary ion current density at the target and S is the bombarded area). I_x and I_p are expressed in units of ions/second. The combined subscript (x, m) for a certain parameter in eq. (7) reflects a possible dependence of that parameter on the nature of both the sputtered entity and the target matrix. Generally, in a description of sputtering from a multi-component system, the influence of preferential sputtering and surface segregation is involved, as the preferential sputtering of a component in a bulk causes a generation of an altered layer with different composition from the bulk. However, in spite of differences in yields of the individual atom species, partial sputtering yield of species (x) is not included in eq. (7), as in the steady-state (i.e. in sputter equilibrium), the surface composition is rearranged so that sputtered flux has a composition identical to that of the bulk material. This is the basic concept underlying all quantitative analytical techniques that monitor the sputtered flux.

Y_{tot} is the global sputtering-yield of the target matrix (total number of atoms of all species sputtered from the matrix per incident ion); an estimation of which can be made following any of the standard techniques of sputter-yield measurements.

$\beta^{\pm}_{x,m}$ is the positive or negative ionization probability of the species (x) sputtered from the matrix (m) and depends strongly on the nature of both the sputtered entity and the local surface chemistry of the sample, thereby causing the greatest difficulty in SIMS quantification. The product ($Y_{tot}.\beta^{\pm}_{x,m}$) is the ion-yield (ratio of the sputtered ion flux of a given species to the incident primary ion flux) of the species (x) sputtered from the target matrix (m).

The well-known characteristics of SIMS is the fact that the ion-yields vary dramatically from element to element. Moreover, the secondary-ion yield for a certain element present in a matrix depends strongly on the presence of other elements in the same matrix. Such a strong dependence of the ionization probability on the surface chemistry is known as "**matrix effect**" and has been evidenced by the fact that the presence of electro-negative species (like oxygen) on a surface enhances the positive ion-yield significantly [14]. The enhancement is larger; the larger is the electro-negativity [15] of the species with respect to the emitted element. For example, fluorine gives a larger positive ion-yield enhancement compared to oxygen of the same concentration. An analogous effect takes place in case of negative ion emission when some electropositive elements (like Cs) are present on the surface. A similar enhancement in positive or negative ion emission occurs when the surface is subjected to oxygen or caesium ion bombardment, respectively. The matrix

effects, however, constitute serious drawbacks on the analytical capabilities of SIMS method, because they are, in general, not very much well characterized and predictable. Therefore, the 'matrix effect' is detrimental in actual quantification and needs to be appropriately compensated.

3.1.1. Compensation of matrix effect

The fractional concentration C_x of the species x (eq. 7) is defined as the ratio n_x/n_m, where n_x is the atomic density for the species (x) in the matrix (m) and n_m is the atomic density of the matrix element itself. Obviously, $C_x = 1$ for a pure single-component matrix. As discussed above, the exact estimation of C_x using eq. 7 is difficult because of the 'matrix effect'. Therefore, the compensation of 'matrix effect' is necessary. Considering only the case of positive ions, eq. (7) can be written as

$$I_x^+ = \rho_x . C_x \tag{8}$$

where ρ_x (= $I_p Y_{tot} \beta_x^+ f$, with f = f(ΔE) f($\Delta\Omega$) $T_{x,m} \eta_{x,m}$) is called the "absolute sensitivity factor" (ASF) for the species x. While undertaking depth profie of a certain species (x), eq. (8) can be expressed as

$$I_x(t) = \rho' n_x(t) \tag{9}$$

where $n_x(t)$ is the atom concentration of x in the sample at a depth z corresponding to a sputtering time t and ρ' is the 'calibration constant'.

In eq. (7), f(ΔE) is the fraction of secondary ions with energies in the range E and E+ΔE entering into the mass spectrometer, f($\Delta\Omega$) is the fraction of secondary ions accepted by the mass spectrometer in a solid angle $\Delta\Omega$), $T_{x,m}$ is the transmission factor of the mass spectrometer for ions of mass m of a species x, and $\eta_{x,m}$ is the detection efficiency of the detector or ion-collection optics for ions of mass m of a species x. The instrumental factor f can be taken as constant for a particular set of mass spectrometer and associated instrumentation. Therefore, the fractional concentration C_x (or the atomic concentration n_x) of the species x in a given matrix m can be estimated from the secondary ion current using eq. (8), provided ρ_x is known.

The 'absolute sensitivity factor' contains the term $\beta^{\pm}_{x,m}$, exact evaluation of which is necessary for quantification. In other words, the matrix effect needs to be compensated. The lowest detectable concentration in a given matrix that can be measured by SIMS is called the detection-limit. In order to eliminate the fluctuations in I_x^+, $\beta^{\pm}$, Y, f etc. and to correct for the matrix effect, secondary ion current is normalized with a reference or matrix current I_m^+ [2]. From eq. (8), the fractional concentration $C_x = I_x^+/\rho_x$

or $C_x = \dfrac{I_x^+}{I_p \, Y \, \beta_x^+ \, f}$ (10)

Similarly, for the matrix m

$C_m = \dfrac{I_m^+}{I_p \, Y \, \beta_m^+ \, f}$ (11)

In order to eliminate the fluctuations in I_x^+, $\beta^\pm$, Y, f etc. and to correct for the matrix effect, secondary ion current is normalized with a reference or matrix current I_m^+ [2]. Therefore, from eqs. (9) and (10),

$(C_x)_{min}/C_m = \left(\dfrac{(I_x^+)_{min}}{I_m^+}\right) / \left(\dfrac{\beta_x^+}{\beta_m^+}\right)$ (12)

or

$(C_x)_{min} = \left(\dfrac{(I_x^+)_{min}}{I_m^+}\right) / \left(\dfrac{\beta_x^+}{\beta_m^+}\right)$ (since $C_m = 1$) (13)

Since I_m or I_{matrix} is related to the material consumption and expressed as $[k.(dz/dt).S]_{matrix}$, the detection-limit or the minimum detectable fractional concentration $(C_x)_{min}$, as obtained from eq. (12), can be expressed as

$(C_x)_{min} = \left(\dfrac{(I_x^+)_{min}}{(k.\frac{dz}{dt}S)_{matrix}}\right) / \left(\dfrac{\beta_x^+}{\beta_m^+}\right)$ (14)

where (dz/dt) is the erosion-rate or layer-thickness sputtered per second, S is the target area hit by the primary beam and k is a constant depending on the sample and the ion-optics of the mass spectrometer. Therefore, atomic density n_x (atoms/cc) of a certain species (x) can be expressed as

$n_x = n_m \dfrac{I_x^+}{I_m^+} / \dfrac{\beta_x^+}{\beta_m^+} = (RSF)_x \dfrac{I_x^+}{I_m^+}$ (15)

where, $(RSF)_x = n_m \dfrac{\beta_m^+}{\beta_x^+}$, defined as "Relative Sensitivity Factor" for a given species (x) in a certain matrix (m). The advantage of RSF over ASF is that the RSF actually takes care of the instantaneous fluctuations in the parameters I_x^+, $\beta^\pm$, Y, f. As obvious from eq. (14), the lowest detectable concentration is inversely proportional to the erosion-rate or material consumed in SIMS depth profiling, thus signifying dynamic SIMS to be of higher detection sensitivity compared to static SIMS. eq. (15) gives an estimation of the atomic concentration of a certain species in a given matrix, provided the value of RSF of that species is known. The value of this factor can be indirectly extracted through a calibration process like 'implantation standard method', which involves accurately preparing of a "local standard" by implanting a controlled quantity of a species (x) with a known dose F_x(atoms/cm^2) into another sample of same matrix. This 'local standard' is then used to calibrate the SIMS signals. The value of $(RSF)_x$ in this method can be calculated by integrating eq. (9) over total sampling time T.

$\int_0^T I_x(t)\,dt = \rho' \left[\int_0^Z n_x(z)\,dz\right] \dfrac{1}{\dot{z}}$ (16)

where, $\dot{z} = \dfrac{dz}{dt}$ is the sputter-erosion rate. From eq. (16),

$\rho' = \dfrac{\int_0^T I_x(t)\,dt}{F_x} \dfrac{z}{T}$ (17)

where $F_x = \left[\int_0^Z n_x(z)\,dz\right]$ (18)

Here, F_x is the total dose of implanting ions. Z is crater-depth measured after the bombardment time, assuming a constant sputter-rate. Eq. (17) gives the value of ρ', thus measured from the SIMS profile (secondary ion-current I_x versus time). As $n_x = I_x/\rho'$ (from eq. (9)), the atomic density n_x of the species x at any depth of the sample can be measured using I_x and the estimated calibration constant ρ'.

Now, from the measured n_x and using eq. (15), $(RSF)_x$ can be expressed as

$(RSF)_x = \dfrac{F_x \, T \, I_m}{Z \int_0^T I_x(t)\,dt}$ (19)

Where, I_m is the secondary-ion current of the matrix element (m). Z is the erosion-induced crater-depth and $\int_0^T I_x(t)\,dt$ is obviously is a measure of the total area under the depth-integral curve of the secondary ion-current I_x over a span of total time of depth-profiling.

There are several other approaches towards quantification without standards. One such is the "infinite velocity approach" [16]. This uses the inverse velocity (1/v) plots obtained from corrected ion intensity (transmission and sputter-corrected secondary-ion yields) of an element in a matrix as a function of the 'inverse of the ion-velocity' calculated directly from the energy distributions of the secondary ions. The basic idea is that the

ionization probability increases exponentially with decreasing 'inverse ion-velocity', and in the limit of infinite velocity, all sputtered ions are fully ionized. That means, the secondary ions with infinite velocities are obviously uninfluenced by the local surface chemistry. Or in other words, the matrix effect is fully removed. However, the difficulty is that the secondary ions have extremely low intensities at the high energy tails of the energy distributions. The kinetic energy distributions of secondary-ions, mostly peaked at few eVs, have quite long ranges extending up to several kiloelectron volts. The ion-intensities in such keV regions drop down to the background level and are almost undetectable. Another interesting approach is the use of slow (few keV/u), highly-charged ions (such as Xe^{44+} and Au^{69+}) as the bombarding species and the study of secondary ion-yields and ionization probabilities. It has been observed that the secondary ion emission in those cases exceeded the values for conventional sputtering with singly-charged ions by orders of magnitude [17]. Furthermore, the ionization probability for secondary positive-ions from UO_2 and GaAs (100) as a function of projectile charge-state has shown a strong decoupling of secondary ion production from ionization probability, making the highly-charged ion-based SIMS technique free from the matrix effect [17].

3.1.2. MCs_n^+ (n = 1, 2, ...) molecular-ions

Although the quantification of a given matrix can be achieved by using 'standards' with matrix composition closest to the unknown composition of sample, it is very complicated to quantify or even interpret the analysis across interfaces composed of matrices of different nature like metal/semiconductor, metal/polymer, metal/ceramic, etc. In view of this, alkali element-based molecular MA^+ - SIMS approach (where A stands for alkali primary-ion, such as K^+, Rb^+, Na^+, Cs^+, etc.) has been found to be remarkable for the reduction of matrix effect [18], thereby making SIMS quantification possible without the aid of calibration standards. Cs^+ primary-ion is chosen in most of the cases for its better reactivity with the sample surface compared to that of other alkali elements and the monitoring of MCs^+ ions in the SIMS analysis is known as MCs^+-SIMS technique [2]. The reduction (or absence) of matrix effect for these species was rationalized by their possible formation/ionization mechanism, namely the combination of a sputtered (neutral) M-atom with a Cs^+ ion in the sputtering event. Here, M is referred to as the element of interest present in the matrix. The Cs atoms generally have very high ion-yields (close to unity) and, in many cases, are present as ions at the surface. Thus, under steady-state conditions, the flux of MCs^+ ions reflects (via that of M-atoms) the atomic concentration of the element M in the matrix. It has been found experimentally that for a variety of semiconductors the yield of these species exhibits a quadratic dependence on the atomic polarizability (α) of the element M (ion-yield $\propto \alpha^n$), where n $\approx$ 2 [19], thus establishing the key-role that the polarizability of M plays role in the formation of MCs^+ molecular-ions. Dependence of the binding strength on the polarizability has been modelled by an interaction potential between an alkali-ion and a neutral atom M of the type (electropositive or electronegative with respect to the alkali element) [20]. In this case the attraction arises between the ion and the ion-induced dipole moment of the neutral species.

The comparative insensitivity of MCs^+ signals towards sample composition was demonstrated by the dependence of the intensities of various secondary ions (Ge^+, Cs^+, $GeCs^+$, $GeOCs^+$, etc.) sputtered from $Ge_{1-x}O_x$ samples on oxygen concentration [21]. While the Ge^+ intensity exhibited a monotonic increase with oxygen concentration, Cs^+ and $GeCs^+$ were found to remain almost invariant. In an additional measurement, the energy distribution of $GeCs^+$ sputtered from a $Ge_{1-x}O_x$ sample was found to be identical to that from a pure Ge sample. The reasonable insensitivity of $GeCs^+$ ion intensity from $Ge_{1-x}O_x$ with varying oxygen concentration and the identical energy spectrum of $GeCs^+$ ions for pure Ge and $Ge_{1-x}O_x$ samples demonstrated the relative inertness of MCs^+ against specimen composition. The MCs^+-SIMS technique was found to be extremely useful while analyzing a metal/semiconductor interface (Fig. 4). A complete absence of 'matrix effect' was found in the analysis of a simple structure of a thin (0.3 μm) gold film grown on a GaAs substrate [18] by monitoring $AuCs^+$ ions. The appearance of a large hump of Au^+ signal across the interface is the characteristic of an interface-peak due to the possible presence of some oxygen or other electronegative species at the interface. This interface-peak invariably caused by 'matrix effect' is successively reduced under different monitoring conditions and has completely disappeared while monitoring $AuCs^+$ signals (Fig. 4e).

The formation mechanisms of MCs^+ molecular-ions in SIMS and the analytical applicability of MCs^+-SIMS technique have been thoroughly examined [22]. Based on all experimental observations, it was proposed that MCs^+ ions form via a recombination of independently sputtered neutral M atoms and Cs^+ ions. For such a formation mechanism to be valid, the intensity ratio $I(MCs^+)/I(Cs^+)$ is expected to vary linearly with the sputtering yield of M and inversely with the mean velocity of M [21],

$$I(MCs^+)/I(Cs^+) \propto Y_M/\langle v_M \rangle \tag{20}$$

where $\langle v_M \rangle$ accounts for the density of M atoms in the combination volume. It has been shown that the normalized MCs^+ intensity follows an exponential dependence on the change in
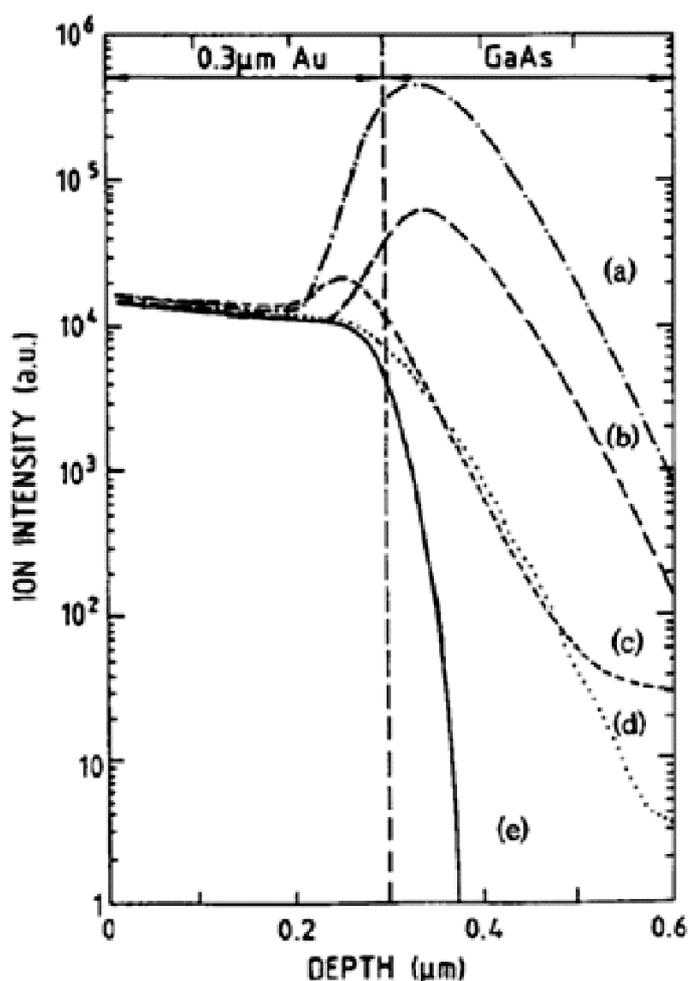
surface work-function [20] and a close agreement between the variation of AgCs$^+$ and Cs$^+$ intensities with the change in surface work-function indicated a direct correlation between Cs$^+$ and MCs$^+$ intensities.

From eq. (5), the ionization probability P$^+$ depends on the ionization potential I of the sputtered atom and surface work function according to the relation

$$P^+ \propto \exp[-(I-\phi)/\varepsilon_0] \qquad (21)$$

where ε_0 is a parameter, related to the normal component of the emission-velocity of the secondary ions. The normalized Cs$^+$ count as a function of the change in surface work-function $\Delta\phi$ showed a very good agreement with the theoretical prediction for $\varepsilon_0 = 0.29$ eV [4]. In the case of silver, under a combined influence of electropositive (caesium) and electronegative (oxygen) elements, the normalized AgCs$^+$ intensity as a function of

normalized Cs$^+$ intensity, showed a linearity, which was in good agreement with the theoretical prediction for all oxygen exposures in the sputter-region [4]. This observation has obviously strengthened the concept that MCs$^+$ formation takes place via a recombination of a sputtered neutral M^0 atom with a re-sputtered Cs$^+$ ion. In this case, the electric field of a Cs$^+$ ion in the close proximity polarizes the neutral M^0 atom causing an interaction between the Cs$^+$ ion and the ion-induced dipole moment of the neutral species M. The intensity of MCs+ molecular ions can be expressed as

$$I_{(MCs+)} = \beta_{Cs}\,(\gamma_{MCs})k_M(C_{Cs}C_M/C_{total}{}^2)(Y_{total})^2I_p \qquad (22)$$

where, γ_{MCs} denotes the recombination coefficient of M^0 with Cs$^+$; C_{Cs}, C_M are the fractional concentrations of Cs and M; C_{total} is the total concentration; Y_{total} is the global sputter-yield; I_p is the primary ion-current; k_M is a constant (≈ 1). The recombination coefficient for MCs$^+$ is found to be greater for elements with higher electro-positivity. Fig. 5 shows the recombination coefficients of MA$^+$ (A – alkali element) for Ga, Al and As(electropositivity in the decreasing order) with different alkali element like Cs, Rb, K and Na. As evident from the figure, the recombination coefficient for GaA$^+$ is highest for any alkali element, compared to that for Al or As. Again,Ga being of strongest electropositivity relative to Na, the recombination coefficient for GaNa$^+$ is highest amongst all combinations.
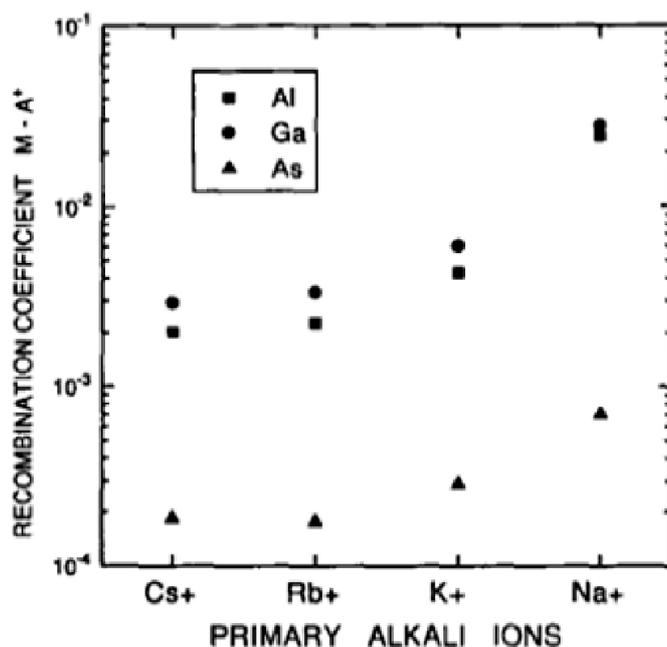

Fig. 5. Recombination coefficient for MA$^+$ (where M stands for Ga, Al and As; A stands for Cs, Rb, K, Na). As evident, the recombination coefficient is greater for elements with higher electro-positivity.

Although MCs$^+$-SIMS approach can explain the absence of pronounced matrix effects, its experimental foundation is still
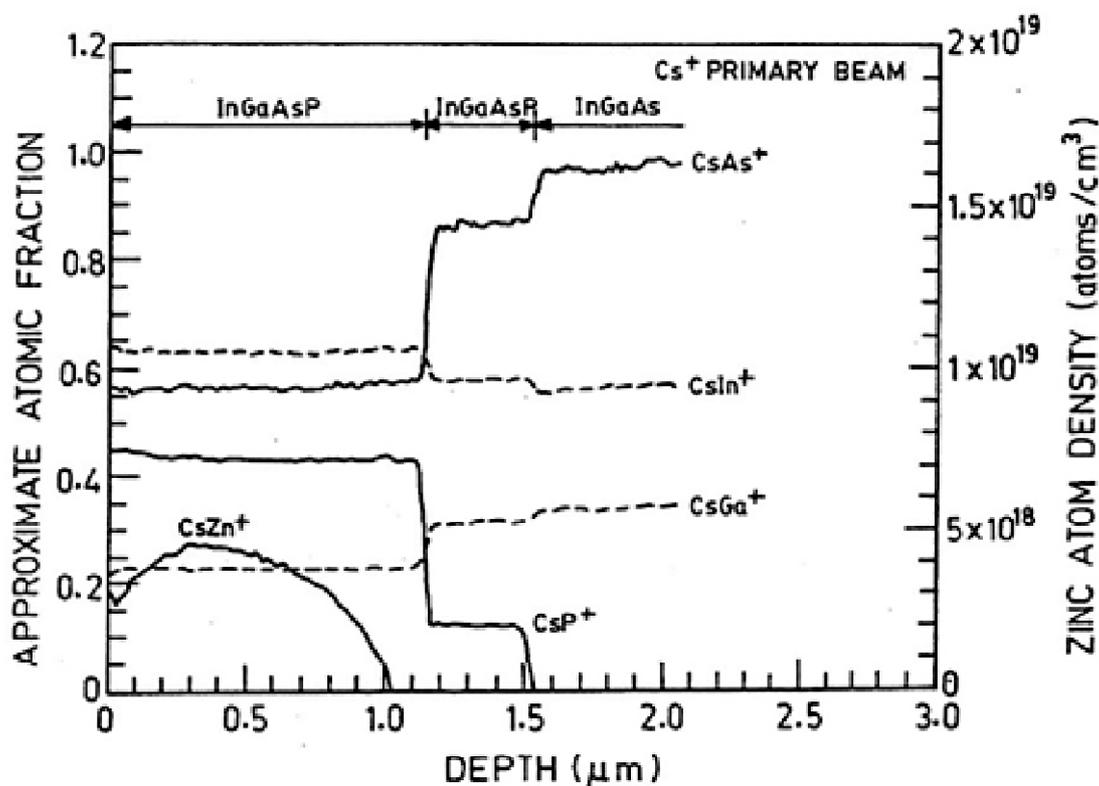
Fig. 6. SIMS depth profiles of a layered sample consisting of two different stoichiometry of InGaAsP on InGaAs, using Cs$^+$ primary ion beam with detection of MCs$^+$. The signals of major elements (In, Ga, As, P) are good representations of their actual densities in the layers [23].

limited. An example for the use of this technique is the depth profile analysis of a Zn-diffused layered sample consisting of InGaAsP of two different stoichiometries on InGaAs substrate [23] (shown in Fig. 6). By using Cs$^+$ primary ions and monitoring MCs$^+$ secondary ions, it was found that the effects of changing matrix on the ion yields of the major elements were minimal, and the signals for the major elements were in good representations of their actual densities in the layers.

Although the MCs$^+$-SIMS approach has found its great applicability in direct quantification without the need of calibration standards, it generally suffers from a low useful yield. In such case, the MCs$_2^+$ molecular-ions offer a better sensitivity as the ion-yields for MCs$_2^+$ molecules have been observed to be much higher than that for MCs$^+$ ions. This is true in most of the cases where the elements are strongly electronegative with respect to caesium. Fig. 7 shows a typical SIMS depth profile analysis of a fluorine-implanted Si-wafer using FCs$^+$ and FCs$_2^+$ molecular-ions. As observed, MCs$_2^+$ ion-yield is higher than that of MCs$^+$ ions by orders of magnitude [18].

As far as the formation mechanisms of MCs$_2^+$ molecular ions are concerned, a handful of works have revealed the underlying formation mechanism these molecular-ions. The study of energy distributions of the MCs$_2^+$ molecular-ions and their constituents

has been the key-probe to understand its formation mechanism [24]. The energy distribution of the MCs$_2^+$ molecules for various elements has been found to depend on the surface binding energy, which provides evidence that the energy distribution of the neutrals is also responsible for the MCs$_2^+$ energy distributions [25]. The formation mechanisms of these molecular ions depend on the nature of the element M. Two possible mechanisms [25] are

$$M_0 + Cs_2^+ \rightarrow MCs_2^+ \tag{23}$$
$$MCs^0 + Cs^+ \rightarrow MCs_2^+ \tag{24}$$

While the first mechanism seems to dominate for electropositive element M, the second one becomes important for electronegative elements, thereby exhibiting the enhanced yield [26] of MCs$_2^+$. The MCs^0 in the formation process (24) results from the neutralization of an MCs$^+$ ion by electron capture [25]. According to process (24), the intensity of MCs$_2^+$ molecular ions can be expressed [22] as

$$I_{MCs_2}{}^+ \propto Y \, c_M Y^2 (c_{Cs})^2 P^+ \, f_{MCs^+} f_{MCs_2^+} \tag{25}$$

where, Y is the global sputter-yield; C$_{Cs}$ is the Cs-concentration in the matrix; C$_M$ is the concentration of M; P$^+$ is the ionization probability of Cs$^+$; f$_{MCs+}$ and f$_{MCs2+}$ are the formation probabili-
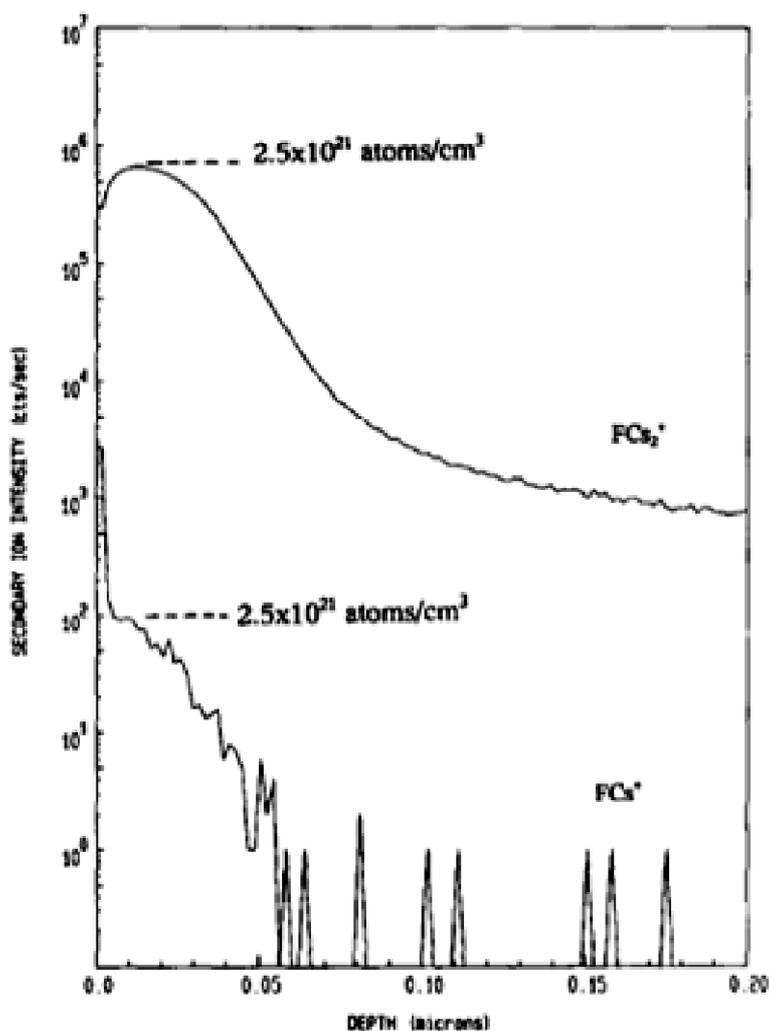
Fig. 7. FCs$^+$ and FCs$_2^+$ ion-profiles for a Si wafer implanted with fluorine at a dose of 8×10^{15} atoms/cm^2. The implantation profile-peak corresponds to a dopant concentrationof 2.5×10^{21} atoms/cm^3, which is almost close to the expected value [18].

ties of MCs$^+$ and MCs$_2^+$ molecular-ions. For a certain element M, c$_M$ and the formation probabilities for MCs$^+$ and MCs$_2^+$ molecular ions can be considered as constant [27]. Therefore, eq. (25) can be rewritten as I$_{MCs2}^+$∝ P$^+$. Thus, the intensity of AgCs$_2^+$molecular ions is expected to vary linearly with the ionization probability of caesium. This has been evidenced with the exponential dependence of normalized AgCs$_2^+$ intensity with the change in surface work function (Δφ) [22]. Those experimental data verified the conjecture that the MCs$_2^+$ molecular ions forms via a recombination of an MCs^0 molecule with a Cs$^+$ ion in the near-surface region (eq. 24). The same argument can be equally applicable for the intensity of MCs$^+$ ions which varies exponentially with the change in surface work function (Δφ) [22]. The formation probability for MCs$_n^+$ (n = 1, 2, …..) is proportional to the spatial and temporal correlation factor of MCs$_n^+$ (n = 1, 2, ….). The proportionality constant is related to the square of the atomic polarizability of M, as expressed in the following [26],
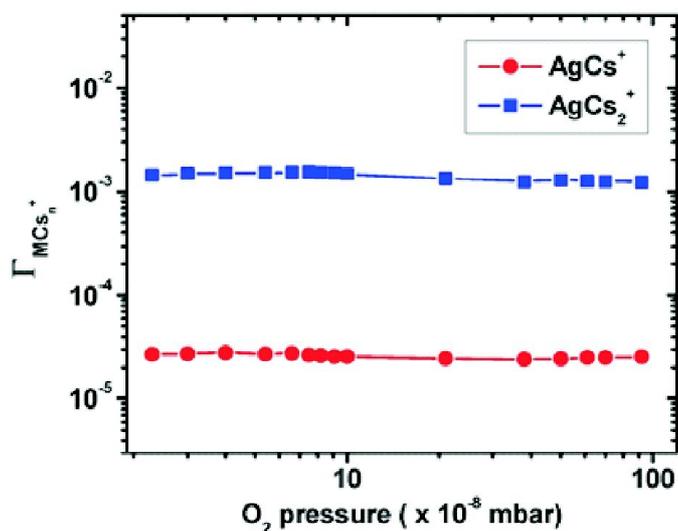

Fig. 8. Formation probabilities (spatial and temporal correlation factor) of MCs$^+$ and MCs$_2^+$ molecular-ions as a function of oxygen pressure in the target chamber [26].

$$f_{MCs_n^+} = \gamma_{M^0}^{pol} \Gamma_{MCs_n^+} \qquad (26)$$

Fig. 8 shows the special and temporal correlation factors for MCs^+ and MCs_2^+ molecular ions for different oxygen environments. As represented, the formation probability for MCs_2^+ molecular-ions is higher than that of MCs^+ ions by two orders of magnitude and both remain unchanged under varying oxygen pressure during the combined influence of oxygen and caesium.

3.2. Composition analysis of multilayered structures and quantum wells

A quantum well is a thin layer of a semiconductor medium, embedded between two other semiconductor layers of wider bandgap (for example, GaAs quantum-well embedded in AlGaAs). Both electrons and holes can be confined in semiconductor quantum wells. This confinement is a quantum effect and has profound effects on the 'density of states' for the confined particles. The effect of "quantum confinement" takes place when the quantum-well thickness becomes comparable to the 'de Broglie wavelength' of the carriers (generally electrons and holes), leading to energy levels called "energy sub-bands", i.e., the carriers can only have discrete energy values. Periodic structures made of two or repeated quantum-wells having barriers too thick for adjacent wave functions to couple, are called double or multiple quantum-well (MQW) structures.

During the analysis of a multilayer structure, special care is taken to obtain the best depth resolution for which the selection of parameters such as high-mass primary beams, low impact energy, high angle of incidence is necessary so as to minimize the erosion-rate. The quantification of matrix constituents in a multilayer structure (e.g. measurement of the value of x in $Al_xGa_{1-x}As$ layers in a GaAs/$Al_xGa_{1-x}As$ multilayer) is complex, as sputter-ion yields vary not only from one matrix to the next but also in an unknown manner in the interfacial regions. It has been shown that for $Al_xGa_{1-x}As$ system the Al^+ and Ga^+ intensities vary linearly with the aluminium content (up to x = 0.5). Based on this observation, the approach is to prepare a series of standard $Al_xGa_{1-x}As$ samples of known compositions and to measure Al^+ and Ga^+ ion intensities from those standards by SIMS. A plot of Al^+/Ga^+ ratios versus (x/1-x) then produces a straight line from which any unknown value of x (Al concentration) and its depth distribution in an $Al_xGa_{1-x}As$ matrix can be determined. This method has many limitations and obviously cannot provide the true compositional profiles of the interfaces in a multilayer structure in general. Depth-resolution can be improved to a great extent by reducing the bombarding-ion energy (which reduces ion-induced collisional mixing) and choosing the correct bombardment conditions, as an additional surface roughening is caused by oblique incidence of the primary beam [2], giving rise to profile broadening. It was shown that the relatively smooth crater bottom collapsed into a pronounced ripple structure [2] for non-normal incidence of the primary beam.

Fig. 9 shows a SIMS depth profile of an 80-period Si/Fe neutron mirror with layers of 1.8 nm thick using normally-incident 1.5 keV O_2^+ primary ions (100 nA). The design conditions of this multilayer structure are fulfilled in order to reach the maximum reflectivity of neutrons, similar to that in layered synthetic microstructures used for the X-UV reflecting devices. The SIMS depth profile shows the layer-thickness to be highly consistent with depth and almost without any degradation in depth-resolution over the entire multilayer structure.
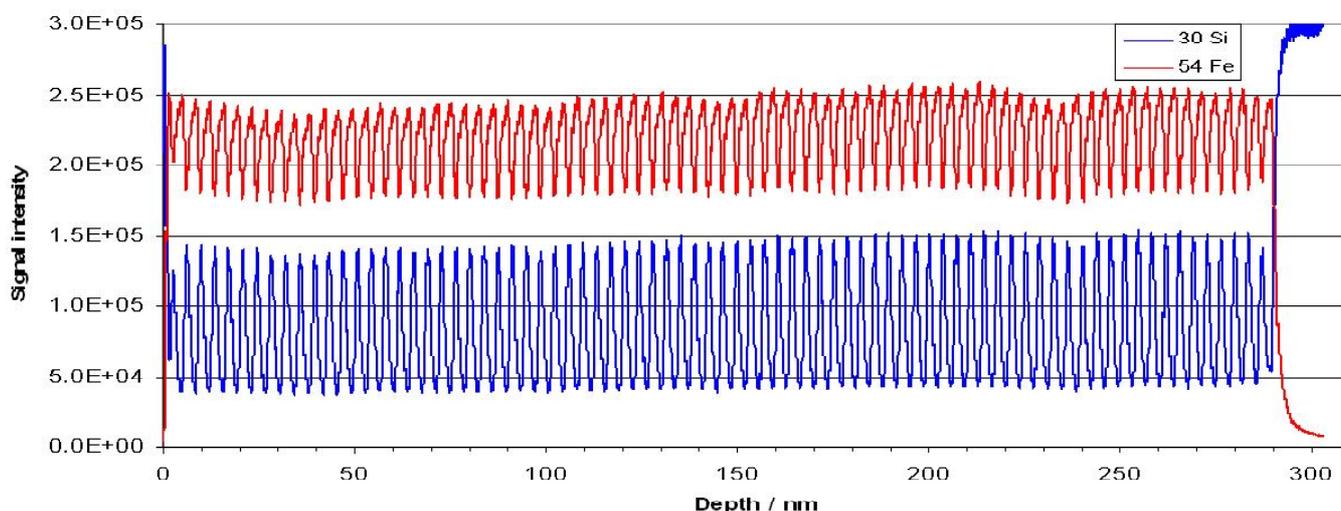

Fig. 9. Depth profile of an 80-period Si/Fe neutron mirror, with layers of 1.8 nm thick, analysed using normally incident 1.5 keV O_2^+ primary ions (100 nA).

3.2.1. Metallic multilayer

In metallic multilayer systems, the large free energies available at the interfaces can help forming interfacial alloys when these free energies are comparable to or larger than the enthalpy of formation of the probable alloy-phases. For multilayers of immiscible metals, there exists a positive mixing enthalpy that acts as an energy barrier to mixing. Whereas for a multilayer of miscible metals, the formation enthalpy for different metastable crystalline or ordered phases are mostly negative and very close to each other. Because of interfacial mixing essentially arising out of interdiffusion, metastable alloys have been found to form across Au/Cu interfaces in a magnetron-sputter grown Au/Cu multilayer structure [28]. Furthermore, sputter-deposition

techniques, because of their high quench-rate and the hyperthermal atoms formed during sputter-deposition were found to be effective in achieving such a situation [28]. It has been shown that an interfacial confinement primarily drives the formation of metastable $D0_{23}$ phase of Cu_3Au alloy across the interfaces of Cu/Au multilayers [28]. Fig. 10 summarizes the observations of such phenomenon. Fig. 10(a) shows the high-resolution cross-sectional TEM image of a 10 bi-layered Cu/Au structure grown on glass substrate and Fig. 10(b) shows the SIMS depth profile of an identical 2 bi-layered Cu/Au structure grown on Si substrate, indicating Au, Cu and Si signals prominently. The depth-resolution of SIMS was good enough to distinguish the various alloy-fragments like AuCu, Cu_2Au and
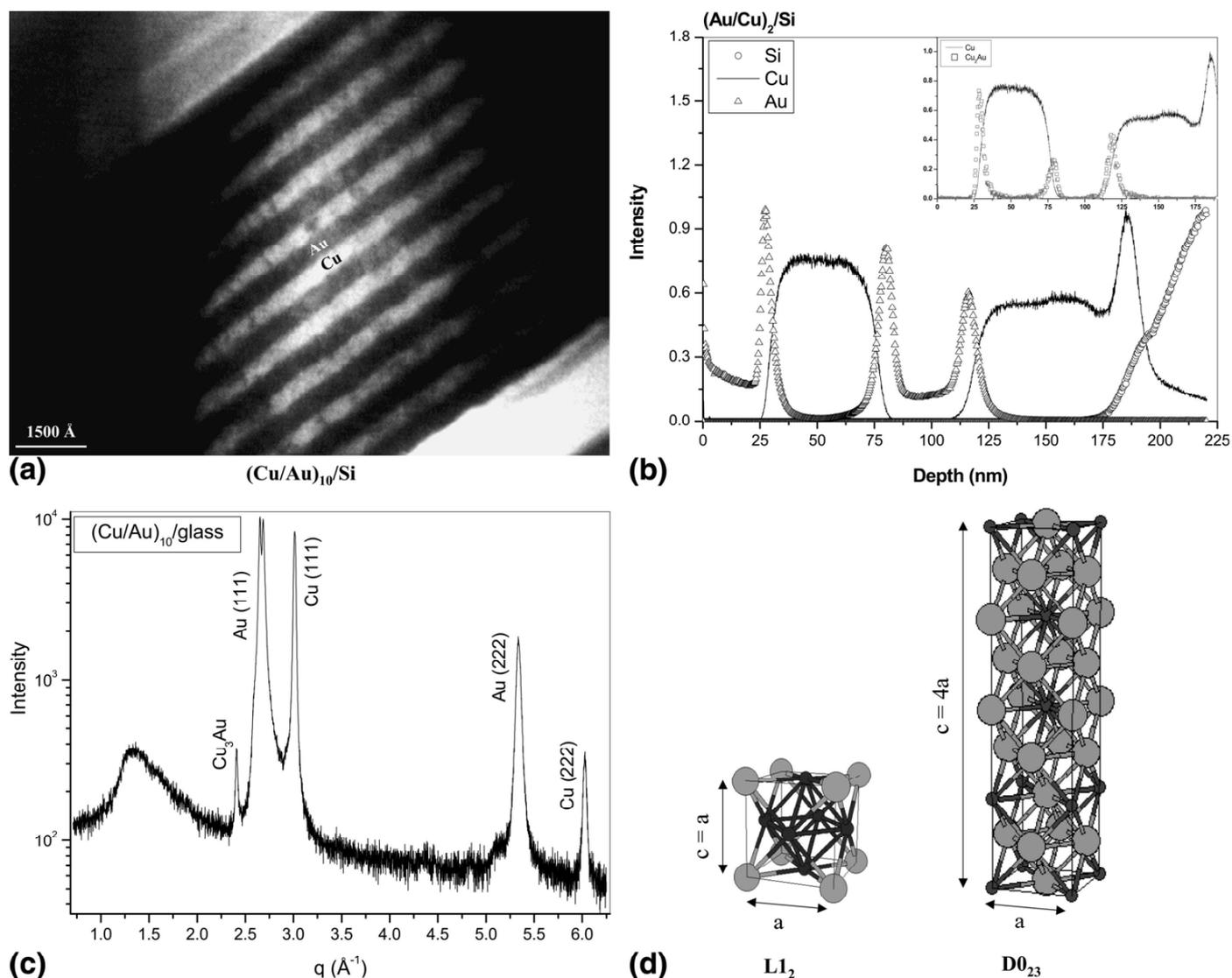

Fig. 10. (a) Cross-sectional TEM image of the $(Cu/Au)10/Si$ multilayer, (b) SIMS depth profiles showing Au, Cu and Si signals in a $(Au/Cu)2/Si$ film, (inset) SIMS depth profiles showing Cu and Cu_2Au alloy fragment signals in the same film, (c) XRD spectrum of the $(Au/Cu)10/glass$ multilayer, and (d) crystal structures of $L1_2$ and $D0_{23}$ phases of Cu_3Au [28].

Au_2Cu that are formed and spatially separated across each interface. One such alloy-fragment like Cu_2Au at the interfaces is indicated in the figure (inset of Fig. 10(b)). Fig. 10(c) presents the XRD spectrum of (Au/Cu)10 /glass multilayer indicating a small sharp peak in the vicinity of Au (111) peak and that new peak is a characteristic of Cu_3Au alloy-phase ($D0_{23}$). Fig. 10(d) represents the crystal structures of L12 and $D0_{23}$ phases of Cu_3Au.

3.2.2. Semiconductor quantum-well

Interdiffusion across the interfaces can cause an interfacial broadening due to intermixing of layers in a quantum well structure. A case study has been presented with a metal organic chemical vapour deposition (MOCVD)-grown $InP/In_{0.33}Ga_{0.67}As/InP/In_{0.33}Ga_{0.67}As/InP$ double quantum well structure through SIMS and XRD along with a simulation programme [29]. Results have shown an interdiffusion of phosphorus into the quantum wells and the presence of a 10 nm thick intermixed zone of In, As and P formed in-between the cap layer and the subsequent quantum well. Combination of these two techniques along with the simulation was found to be a novel approach towards the understanding and quantification of in-depth compositional variation in quantum wells and thin films, in general. In-content in InP layers being already at its maximum, the interdiffusion of In from QWs to InP layers can be ruled out. Therefore, phosphorus from InP-layers can only inter-diffuse into the QWs. This is supported by the shallow valley of the P signal in the QW layers. The peaks of Ga and As have identical width and appear exactly at the same depth in the SIMS profile (Fig. 11), reflecting the identity of double quantum-well structure.

A high-resolution x-ray diffraction experiment can provide an estimate of the stoichiometry of the composition in the quantum well layers through the measurement of absolute lattice parameters of the substrate and the phases grown in the deposited layers. A simulation programme, based on the 'kinematic theory of reflection' [30], was developed to reproduce the experimental high-resolution diffraction pattern of the double quantum well in the Born approximationscheme [29]. The interplanar spacings were obtained from the measured X-ray data. The scattering amplitude needed for simulation depends on the relative concentration of the elements present in the sample, and thus would change with depth throughout the stack due to the variation of in-depth elemental composition. From the study of high-resolution XRD around the (004) Bragg peak as a function of q_z (= $(4\pi/\lambda)$ $\sin\theta$), interplanar spacings (d-values) in $In_{0.33}Ga_{0.67}As$ and InP layers were determined to be around 1.428 Å and 1.495 Å, respectively. Applying the Vegard's law [31] for a quaternary material like $A_{1-x}B_xC_yD_{1-y}$ constructed of four binary compounds like AC, AD, BC and BD, a 'quaternary material parameter' was framed that was essentially regarded as the interplanar spacing, which varies almost linearly with the stoichiometry of the material composition. Applying the above
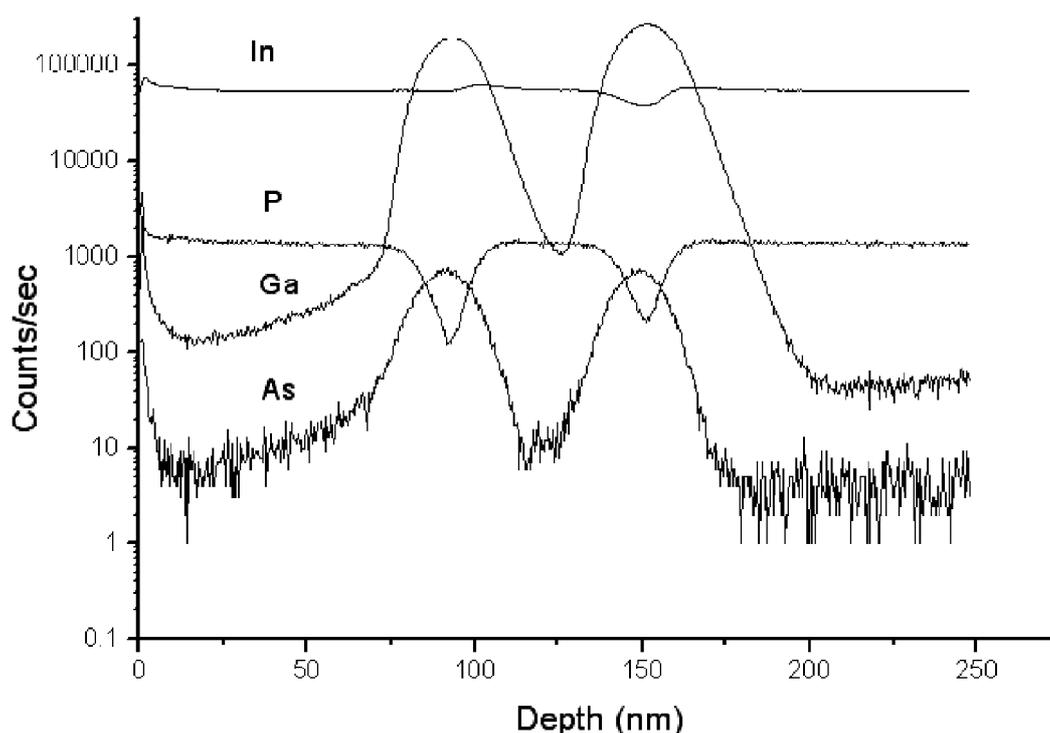

Fig. 11. SIMS depth profiles of In, P, Ga and As in an $InP/In_{0.33}Ga_{0.67}As/InP/In_{0.33}Ga_{0.67}As/InP$ double quantum-well structure [29].

law, the desired composition $In_{0.33}Ga_{0.67}As$ of the QWs cannot have the interplanar spacing of 1.428 Å in the (004) direction. On the contrary, assuming the proportions of In and Ga to remain unaltered and an interdiffusion of phosphorus into the QWs, a reconstructed composition, such as $In_{0.33}Ga_{0.67}As_{0.62}P_{0.38}$, was rather found to match well with the estimated interplanar-spacing of 1.428 Å [29].

3.2.2.1. Reconstruction of depth profiles: MRI simulation

An interesting observation in the SIMS depth profiles of semiconductor multilayer structures is the asymmetry in 'leading' and 'trailing' parts. The leading curve is, in general, steeper than the trailing curve. Such an asymmetry in slopes was found to be quite prominent in the sputter-profiling of a delta-layer (AlAs monolayer on GaAs) and was explained using **MRI** (**M**ixing, **R**ange and **I**nformation-depth) model-fit [32]. With negligible preferential sputtering, the slope of the leading part of a delta-layer was mainly determined by roughness in combination with the information depth, whereas the trailing slope was mainly determined by the extent of the atomic mixing zone [32].The **MRI** model is essentially a semi-empirical model for depth resolution function (DRF) and was developed using three fundamental parameters: atomic Mixing (w), surface Roughness (σ) and Information depth (λ). "Atomic mixing" is considered to create instantaneously a homogeneously mixed zone of thickness w by complete atomic redistribution. "Surface roughness" is taken into account by a Gaussian term with a standard deviation σ. The "information depth" is characterized by an exponential term with the characteristic mean escape-depth λ of the analytical information (escape-depth in SIMS is the mean escape depth of secondary ions and typically ~1-2 monolayer). The MRI model is characterized by three partial resolution functions of these three fundamental parameters (w, σ, λ), such as f(w), f(σ) and f(λ), which act physically on each other to establish the complete DRF and its role in profile reconstruction. Appropriate choice of these three parameters of the **MRI** model in respect of the specific experimental conditions enable the prediction of the depth-resolution function [2]. By a reasonable set of parameters, such as mixing (w) = 1.0 nm, surface roughness (σ) = 0.6 nm, Auger electron escape depth (λ) = 0.4 nm (Al 68 eV) and λ = 1.7 nm (Al 1396 eV) for 600 eV Ar^+ ion-sputtering, the MRI model was found to give an excellent fit with the measured AES depth profiles of a GaAs (8.8 nm)/AlAs (9.9 nm) superlattice structure [33].

Fig. 12 represents the extracted Al-concentration (mole fraction) in a $GaAs/Al_{0.2}Ga_{0.8}As/GaAs$ multiple quantum-well (MQW) structure through SIMS depth profile using 1.5 keV Cs^+ primary-ions. As evident in the figure, the MRI-convoluted profile per-
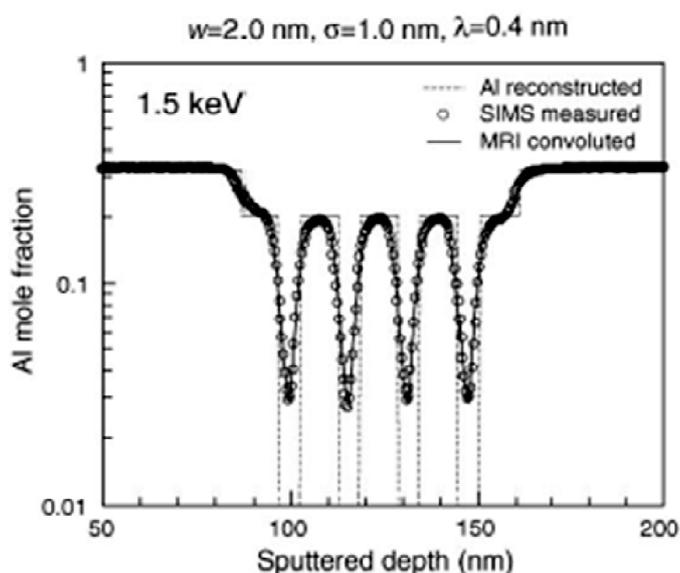

Fig. 12. Al-concentration as a function of depth in a $GaAs/Al_{0.2}Ga_{0.8}As/$ $GaAs$ multiple quantum-well (MQW) structure, fitted with **MRI** (mixing, roughness, information) model.The simulated values: w (atomic mixing) = 2.0 nm, σ (surface roughness) = 1.0 nm, λ (information depth) = 0.4 nm.

fectly matches with the actual SIMS profile. The reconstructed Al profile gives an accurate measure of the quantum-well layer-thicknesses, with a difference between the sputtering-rates of GaAs and $Al_{0.3}Ga_{0.7}As$ within ~5%.

3.2.3. SiGe alloy and Si/Ge superlattice structures: Composition analysis using MCs^+-SIMS approach

SiGe alloy, owing to its high electron and hole mobility, has potential applications in high-speed microelectronic device technology. The optimization of such technology requires the precise determination of Ge concentration in the full range of composition and the understanding and control of the Ge–Si interdiffusion phenomenon. The MCs^+-SIMS method was successfully used for the analysis of Ge concentration up to 23.5% [34] in SiGe alloys. Quantification in the higher range of Ge concentration in SiGe at low sputtering energies was also reported using MCs^+-SIMS [35–37]. However, reliable results of analysis with MCs^+-SIMS method were not reported for SiGe layers with Ge contents higher than 50 at%. A procedure for the accurate quantification of Ge concentration in molecular beam epitaxy (MBE)-grown $Si_{1-x}Ge_x$ (0 <x< 0.72) alloys based on MCs^+-SIMS approach was proposed, in which the "matrix effect" was shown to be completely suppressed for all Ge concentrations irrespective of incident Cs^+ ion energies [38]. The novel methodology was successfully applied for direct quantitative composition analysis of Si/Ge multilayer structure [38].The lattice parameters extracted from the alloy-peaks in the X-ray diffraction

were utilized to estimate the alloy compositions using Vegard's law. The results were found to be in good agreement with that obtained independently from energy-dispersive X-ray analysis (EDX).

The MCs$^+$ intensity in the MCS$^+$-SIMS for a species M is given by [39]

$$I_{MCs^+} \propto Y \, c_M Y \, c_{Cs} P^+ f_{MCs^+} \tag{27}$$

where Y, P$^+$ and f$_{MCs^+}$ are the total sputtering yield, ionization probability of caesium, and formation probability of MCs$^+$ molecular-ions, respectively. c_M and c_{Cs} are the fractional surface-concentrations of the species M (matrix) and caesium, respectively. Considering the constancy of the formation probability f$_{MCs^+}$ for both germanium and silicon, eq. (27) can be rewritten as

$$\frac{I_{GeCs^+}}{I_{SiCs^+}} = K \frac{c_{Ge}}{c_{Si}} \tag{28}$$

where K is a constant which can be treated as the "relative sensitivity factor" (RSF) for compositional analysis using MCs$^+$-SIMS approach. Fig. 13 shows the intensity-ratios (I$_{GeCs+}$/I$_{SiCs+}$) obtained from MCs$^+$-SIMS as a function of the concentration-ratios (c$_{Ge}$/c$_{Si}$) obtained from EDX for various ion-impact energies [38]. The Linearity of the graphs, irrespective of germanium and silicon contents in SIGe alloy-films for all ion-energies, clearly reveals the absence of "matrix effect" for all possible Si$_{1-x}$Ge$_x$ compositions; whereas some study reported the absence of matrix effect for impact energy only lower than 1 keV and for germanium content less than 50% [40]. The complete compensation of matrix effect irrespective of impact ion-energy was attributed to low steady-state surface concentration of caesium due to larger primary impact angle [38], signifying the achievement of MCs$^+$-SIMS technique in quantitative materials analysis without the aid of calibration standards. The linearity of the graph I$_{GeCs+}$/I$_{SiCs+}$ as a function of c$_{Ge}$/c$_{Si}$ in the case of MCs$_2$$^+$-SIMS analysis provided much better perception in respect of its slope, compared to that in the case of MCs$^+$-SIMS analysis. Fig. 14 shows the plots of (I$_{GeCs+}$/I$_{SiCs+}$) as a function of (c$_{Ge}$/c$_{Si}$) for a set of standard Ge$_x$Si$_{1-x}$ samples in the MCs$^+$-SIMS and MCs$_2$$^+$-SIMS analysis modes. As evident, there is one-to-one match between intensity ratios (GeCs$^+$/SiCs$^+$) and concentration ratios (c$_{Ge}$/c$_{Si}$) in the case of MCs$_2$$^+$-SIMS analysis.

The potential of MCs$^+$-SIMS approach was applied for direct compositional analysis of an MBE-grown Si/Ge multilayer structure, with a nominal thickness ~10 nm for each Si/Ge bilayer [38]. Using eq. (28), the RSFs for Ge were calculated from the slopes of the variation of I$_{GeCs+}$/I$_{SiCs+}$ (MCs$^+$-SIMS approach) with c$_{Si}$/c$_{Ge}$ (EDX) for different ion-impact energies. From the concentration profiles obtained through MCs$^+$-SIMS, the electron density profile ρ$_e$ as a function of thickness (z) of the multilayer was obtained using the following expression[38],

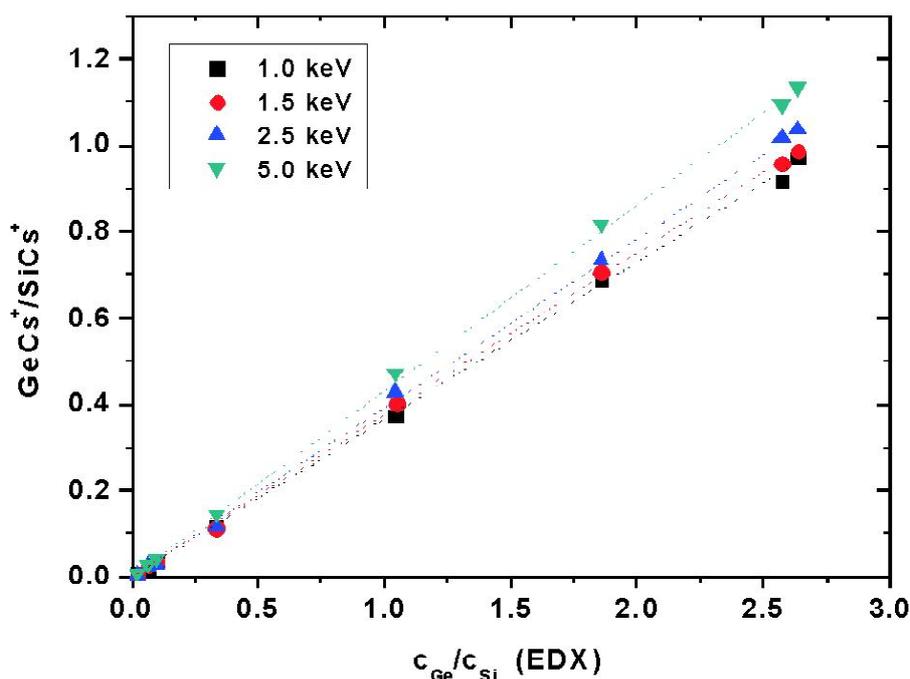$$\rho_e(z) = N_A \sum_{M=Ge,Si} \frac{Z_M C_M(z)}{A_M} \tag{29}$$

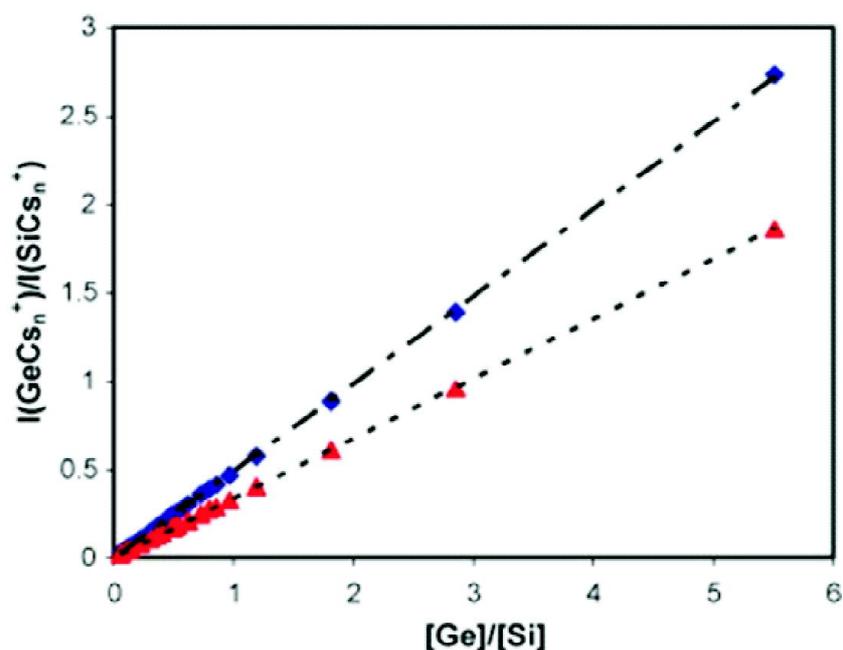**Fig. 13.** Normalized GeCs$^+$ intensity as a function of germanium concentration ratio [38].

Fig. 14. Plots of I_{GeCs+}/I_{SiCs+} as a function of c_{Ge}/c_{Si} for a set of standard Ge_xSi_{1-x} samples. The red solid triangles represent for MCS^+-SIMS and black solid squares represent for MCs_2^+-SIMS.

where N_A, Z_M, $c_M(z)$, and A_M are the Avogadro number, atomic number, concentration profile for Ge, Si and mass number of the constituent element M (Ge and Si), respectively. Fig. 15 represents the extracted electron density profile (EDP) (red circles) of the multilayer-stack utilizing the MCs^+-SIMS data and the blue solid line represents EDP of the same multilayer extracted independently from the X-ray reflectivity (XRR) study [41]. As obvious from Fig. 15, the interface positions of the multilayer-stack are well reflected from these two measurements.

However, the discrepancy between the absolute values of the electron densities obtained from XRR and MCS^+-SIMS measurements was attributed to a possible intermixing of Si and Ge occurring across the interfaces of the multilayer-stack during SIMS analysis [38].

4. ZnO nanowalls and ZnS/ZnO hetero-structured nanowalls: Understanding through MCs^+-SIMS analysis

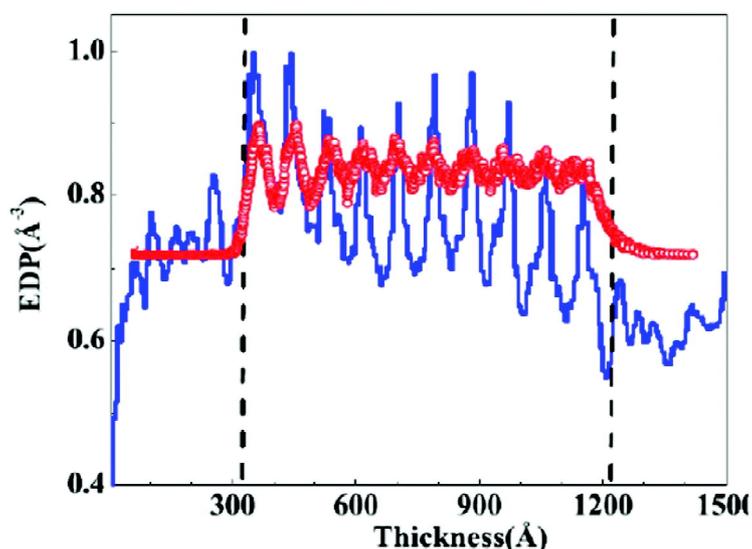In the bare ZnO nanowalls, the sputtering of Zn-atoms through

Fig. 15. Electron-density profiles of 10 Si/Ge bilayers, as obtained from X-ray reflectivity (blue solid line) and MCs^+- SIMS (red circles). Two vertical dashed lines indicate the depth positions for expected buffer and cap-layers [38].

breaking of the oxide-bonds forms oxygen-surrounded vacancies at the surface. These oxygen-surrounded vacancies strongly attract the electrons at the expense of the ejected Zn^+ ions, causing an enhancement in the secondary positive ion yield. An extensive study on the thermal effect on the microstructural modifications of self-assembled ZnO nanowalls grown on Al-substrates was reported [42]. X-Ray diffraction study ensured the formation of hexagonal wurtzite crystal structure of ZnO and the formation of Al_2O_3 layer at the interfaces of Al-substrate and ZnO nanowalls. Fig. 16 represents the SIMS spectra for Zn^+ emission from unannealed and vacuum-annealed ZnO nanowalls grown on Zn-substrate, showing no appreciable change in the Zn^+ intensity under thermal treatment [42]. The luminescence features of ZnO nanowalls were found to be dependent on the presence of surface-adsorbates like O_2^- and OH^- whose presence were ascertained through SIMS. The large deficiency of lattice-oxygen in the vacuum-annealed nanowalls compared to the unannealed nanowalls was also established by SIMS analysis [42]. A phenomena of modified light emission and detection features of SnO-coated ZnO needle-like nanostructures was extensively investigated, where the formation of SnO-phase on ZnO surface was revealed through EDX and SIMS analysis [43].

The 'matrix effect' was found to be prominent during SIMS analysis of the bare ZnO and hetero-structured ZnS/ZnO nanowalls indicating the presence of ZnS-phase over ZnO surface. The 'MCs$^+$ -SIMS' technique was therefore employed to suppress the matrix effect and was found to be potentially effective in making a semi-quantitative estimation of Zn and O surface–atom concentrations in both systems [44]. The lowering of local surface work-function in the heterostructure, as extracted through SIMS, supported the presence of sulfur-species of ZnS on the top of ZnO nanowalls. The higher electron-density in the sulfide-surface lowers the local surface work-function leading to the lowering of positive ionization-probability, there by reducing the Zn^+ ion-intensity in the ZnS/ZnO nanowalls. The "matrix effect compensated MCs$^+$-SIMS" provided a comprehensive understanding of the overall surface-chemistry of ZnS nanoparticle-decorated ZnO nanowalls (ZnS/ZnO heterostructure systems) [44].

The luminescence responses of the ZnS/ZnO hetero-structures were found to be strongly dependent on the extent of ZnS-phase over ZnO. The higher luminescence responses in such heterostructures fabricated with smaller ZnS nanoparticles were explained in terms of a mechanism of charge-carrier transfer from ZnS to ZnO [44]. Fig. 17 represents the SEM images and EDX spectra of the bare ZnO nanowalls and ZnS/ZnO hetero-structured nanowalls. The magnified SEM image in Fig. 17(e) clearly depicts the ZnS nanostructure formation over the top of ZnO nanowalls. Fig. 18 represents the depth-distributions of the intensity-ratio of $ZnCs^+$ and OCs^+ molecular-ions in the MCs$^+$-SIMS analysis mode. The intensities of secondary $ZnCs^+$ and OCs^+ ions were found to be quite steady with depth indicating the homogeneity of ZnO film, while the variation in the intensity of SCs^+ indicated the transitory existence of ZnS in the heterostructure network. Since for MCs$^+$ molecular-ions,

$$\frac{I_{ZnCs^+}}{I_{OCs^+}} \propto \frac{C_{Zn}}{C_O}$$, the higher value of the ratio I_{ZnCs+}/I_{OCs+} indicates the higher concentration ratio c_{Zn}/c_O. This indicates the
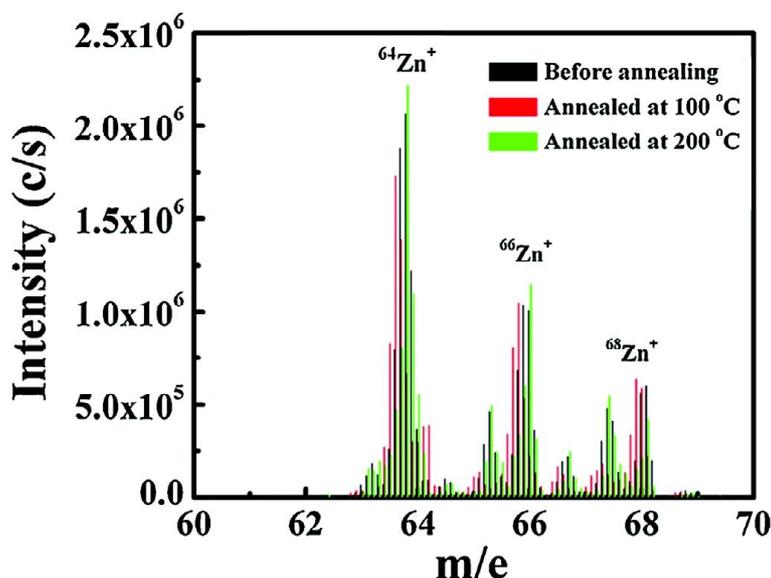

Fig. 16. SIMS spectra for Zn^+ ion-emission from unannealed and vacuum-annealed ZnO nanowalls [42].
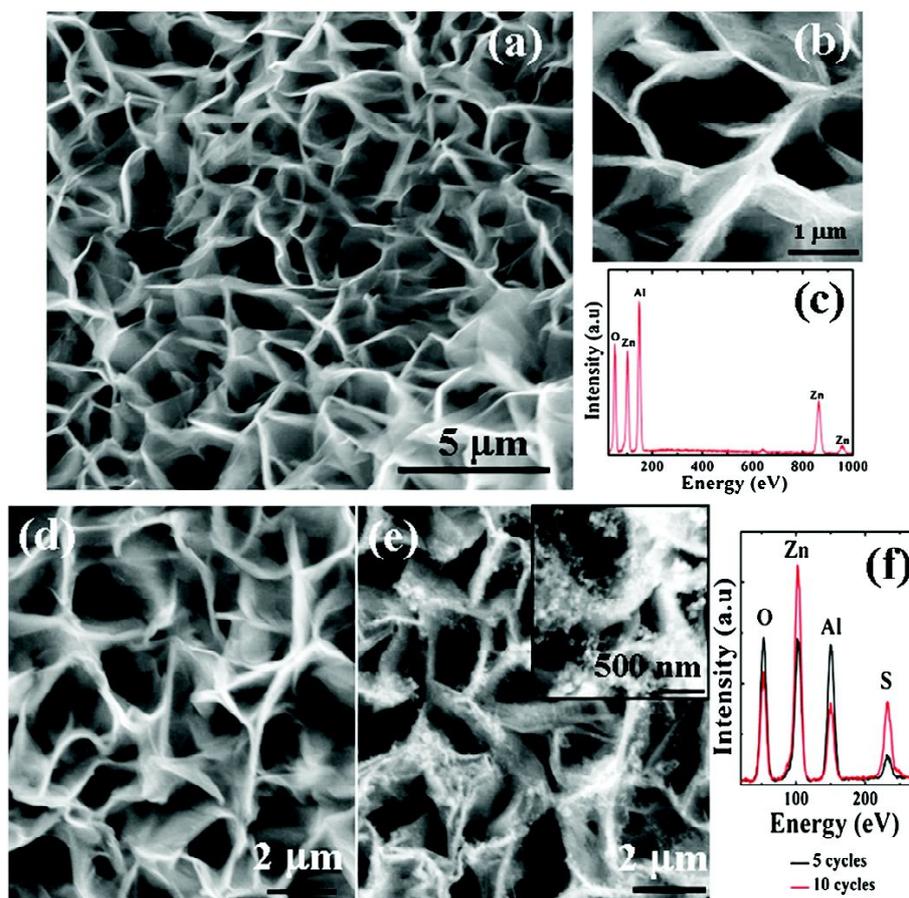
Fig. 17. (a) SEM image of the ZnO nanowall film, (b) magnified image of the nanowalls, and (c) EDX spectra of the nanowalls. (d, e) SEM images of the nanowalls after ZnS growth in 5 and 10 cycles. Inset of (e) depicts the magnified view of ZnS nanostructure formation over the top of ZnO nanowalls. (f) EDX spectra of the ZnS-decorated ZnO nanowalls [44].

increase in Zn concentration compared to O due to the ZnS decoration on the top of ZnO surface (Fig. 18).

Another interesting work was reported on the improved visible light photocatalytic activity in oxygen-deficient TiO_2 nanotubes by narrowing of band gap and effective charge-carrier separation [45]. The performance of TiO_2 under visible light largely depends on its morphology, surface properties, crystal facets, presence of crystalline defects, etc. Doping-induced disorder of the TiO_2 surfaces extends its light absorption in the visible region [46,47]. Doping of non-metal or metal ions into TiO_2 introduces new electronic states into the band gap of TiO_2 making it narrower and also introduces lattice-defects into TiO_2. These defects act as carrier-recombination centres. The oxygen vacancies, introduced into hydrothermally-processed TiO_2 nanotubes by vacuum calcination, modified the local coordination in TiO_2, as revealed by Raman spectroscopy and SIMS [45]. Fig. 19 presents the TEM images of pure (TT) and degraded (DTT) TiO_2. The
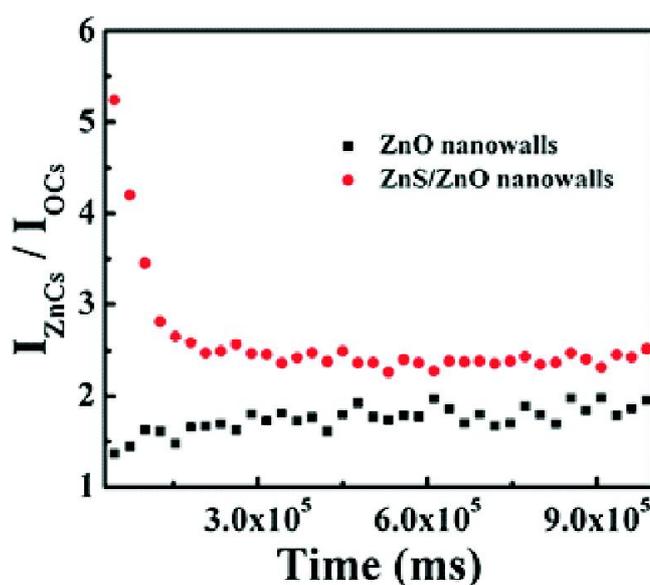

Fig. 18. Variation of intensity-ratio of $ZnCs^+$-to-OCs^+ molecular-ions with sputtering time [44].

high-resolution TEM images of TT and DTT show inner and outer diameter of the nanotubes.
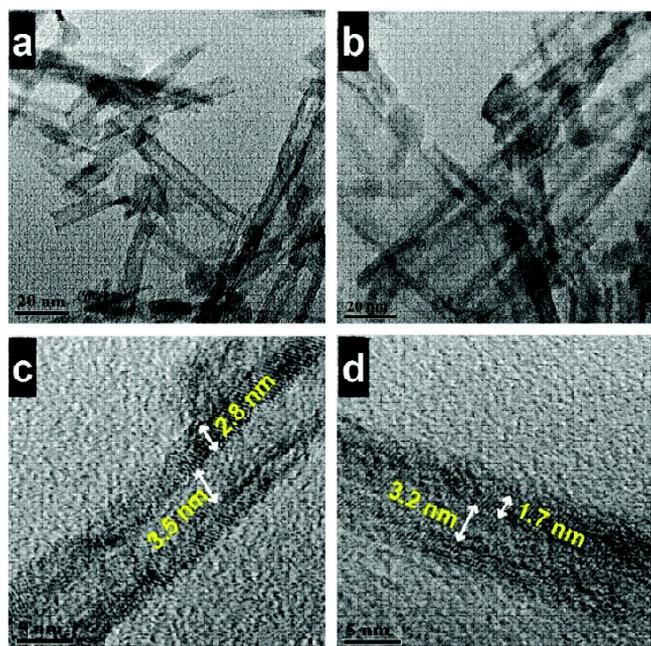

Fig. 19. TEM images of (a) pure TiO_2 (TT) and (b) degraded TiO_2 (DTT). High-resolution TEM images of (c) TT and (d) DTT show inner and outer diameter of the nanotubes [45].

In such a degraded crystalline system, the sputtering-yield is expected to be higher as the bonds can be broken more easily. So, the highest Ti^+ emission was ascribed to the increase in global sputtering-yield of titanium from disordered TiO_2 nanostructures under vacuum calcination. Similarly, the highest $^{64}TiO^+$ emission (Fig. 20) in case of vacuum-calcined TiO_2 system was explained to be due to the increased sputter-emission of TiO-fragments because of the relatively poor crystalline quality of the system under vacuum calcination. However, in contrast to the Ti^+ emission, TiO^+ emission in the case of air-calcined sample was found to be slightly lower compared to that in uncalcined sample confirming the idea that air-calcination leads to the improvement in crystal quality of the TiO_2 nanotubes. The emission of other isotopes of Ti, such as ^{49}Ti and its corresponding oxide ^{65}TiO, followed the similar trend in the SIMS measurements [45].

The photocatalytic activity of nanostructures essentially originates from the native defect-states and is largely influenced by the surface-adsorbants. In a recent work, extensive SIMS study of ZnO nanostructures (nanowires, nanowalls, etc.) have been correlated to their photocatalytic responses [48]. The presence of surface-adsorbed H^+, O_2^-, and OH^- species on the surfaces of nanostructures and the relative changes in substrate
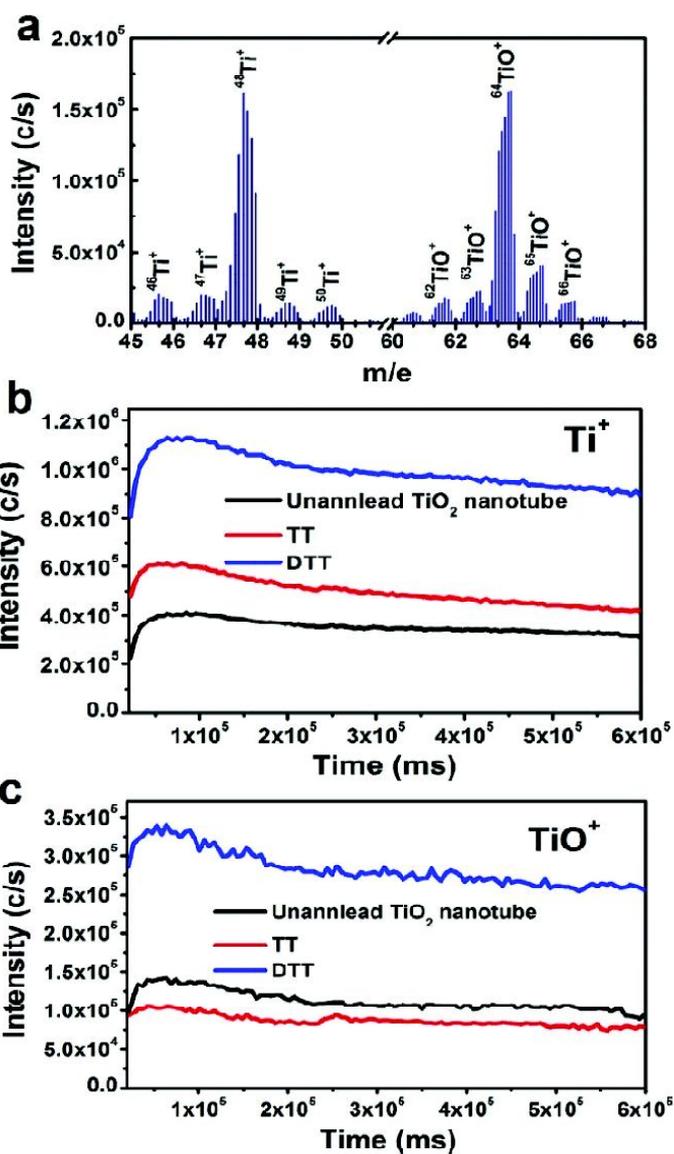

Fig. 20. (a) SIMS spectrum un-calcined TiO_2 nanotube (b) SIMS-depth profiling of Ti^+ and (c) TiO^+ for unannealed, air-annealed and vacuum-annealed TiO_2 nanotube [45].

coverage under varying reaction time have been evidenced through SIMS and substantiated by SEM observation. Compared to nanowires, oxygen adsorption on ZnO surfaces and subsequent oxygen in-diffusion have been found more prominent for the nanowall-like structures and highest for nanowalls grown in lower reaction time. Furthermore, nanowalls have been found to exhibit higher photocatalytic activities, which have been attributed to higher adsorption of oxygen [48].

Conclusion

The unique combination of its highest detection-sensitivity and exceptional depth-resolution has made a great success in the analysis of low-dimensional materials, interfaces of thin films

and superlattices. Time-of-Flight (ToF)-SIMS is highly surface-sensitive, able to provide both elemental composition and molecular information on a surface as well as in-depth. It has the potential to provide detailed insight into the 3D chemical composition for a large mass-range (0 – 10,000 amu) for all elements in the periodic table, organics (polymer, small molecules) and biological materials. On the other hand, dynamic SIMS has the highest detection sensitivity (below parts per billion) and is used to determine the elemental composition and the levels of ultra-trace impurities and dopants in solid materials at any depth.

However, the major limitation of SIMS lies in the quantification owing to its strong 'matrix effect'. Although quantification in a given matrix is achieved by using 'calibration standards', it is very difficult to quantify the cross-interfaces composed of matrices of different nature. Continuous attempts have been made towards exploring the possibilities of 'matrix effect minimization' so that the accurate quantification is possible without the use of calibration standards. Out of several existing techniques for achieving reduced or no matrix effect, the MCs_n^+-SIMS (n = 1, 2, ……) approach using MCs_n^+ molecular-ions is the most useful and beneficial for the precise quantification of quantum structures. In parallel, considerable attempts have been made to conceptually understand the formation mechanisms of these MCs_n^+ molecular-ions through theoretical models.

Since SIMS is essentially a sputter-depth profiling technique, it is very important to consider the most significant detrimental effects, such as 'surface roughening', 'ion-beam induced atomic mixing' and 'broadening in the information-depth' for the correct evaluation and quantification of depth profiles across the interfaces even under optimized experimental conditions. An understanding and accurate estimation of these three fundamental parameters using **MRI** (**M**ixing, **R**oughening, **I**nformation depth) simulation model is extremely useful to construct a depth-resolution function (DRF) which has a significant role in depth profile reconstruction. However, the effects due to nonlinear behaviour such as preferential sputtering, interface segregation, etc. are not yet fully understood so as to make more refined prediction of DRF.

Interface analysis of multilayers is of continued interest in materials science. In particular, problems in semiconductor technology have been a driving force. Dynamic SIMS has shown its tremendous applications in various multilayer systems including semiconductor Bragg mirrors and quantum wells. Interfacial diffusion across interfaces is a natural process causing compositional changes across the interfaces in layered structures. In combination with other measurements like x-ray reflectivity, x-ray diffraction, etc. dynamic SIMS has been found to be useful for compositional analysis of the interfaces in

semiconductor multilayers. In metallic multilayers, the formation of interfacial alloys can exhibit various crystalline structures. The structure of a particular alloy-phase at interface is determined by many parameters, interfacial energies, composition and ordering condition. Moreover, the strong confinement effect at the interfaces may give rise to a novel interfacial alloy phase that could have a crystal structure completely different from that in the bulk. SIMS and XRD analyses together can effectively probe such novel 'interfacial alloys' in metallic multilayer systems.

Although there have been enormous instrumental and methodological developments in SIMS for surface and interface analysis in condensed matter systems in general, futuristic application range of this sputter-induced surface analytical technique is not very clear at this moment. An in-situ SIMS analysis with an extreme level of optimization in depth resolution during a controlled film growth will be a useful attempt to make a real-time analysis of an interface providing a much better understanding of the interfacial behaviour. Furthermore, adequate flexibility and improvisation in the SIMS instrumentation could possibly lead to an extension of this technique towards another direction, for example, the analysis of the instantaneous 'layering of liquid' or 'surface melting' states. Of course, multi-technique approaches are very much essential in which a novel combination of SIMS with other analytical techniques can be useful for the analysis of complex soft condensed matter systems such as colloids, functional materials, supra-molecular assemblies, liquid crystals, crystalline polymers, granular media, photonic matamaterials, etc.

Photonic metamaterials have emerged as engineered optical materials containing nanostructures which give remarkable optical properties. These structures are made from at least two different materials, often involving both metals and dielectrics. They are normally periodic, with the period being small compared to the optical wavelength. Therefore, the special optical properties do not arise from photonic bandgaps as for certain photonic crystals, but rather from an interaction similar to that of atoms or ions in a normal solid medium. These artificial electromagnetic materials of subwavelength periodicity have negative refractive index($n_1 < 0$) that behave contrary to the conventional "right-handed" interaction of light found in conventional optical materials. Hence, these are often called as left-handed materials or negative index materials. Shelly, et al. presented an experimental scattering data at microwave frequencies on a structured metamaterial that exhibits a frequency band where the effective index of refraction is negative [49]. Hoffmann et al [50] reported a novel class of semiconductor metamaterials that exhibit a strongly anisotropic dielectric function to achieve negative refraction in the mid-infrared region (~8.5–13 μm) of the spectrum. They presented highly doped quantum-well

superlattices that are highly anisotropic. Using transmission and reflection measurements and modelling of the highly-doped quantum-well superlattices, they demonstrated anomalous reflection due to the strong anisotropy of the material. This new class of semiconductor metamaterials has great potential in materials science, especially for waveguiding and imaging applications in the long-wave infrared region.

References

[1] Brundle CR, Evans CA, Wilson S. "Encyclopaedia of materials characterization", (Butterworth-Heinemann, Boston, 1992).

[2] Chakraborty Purushottam, in Ion Beam Analysis of Surfaces and Interfaces of Condensed Matter Systems (Ed. Chakraborty Purushottam), Nova Science, New York, 2002.

[3] Oechsner H, Gerhard W. Phys. Lett. 1972;A40,211.

[4] Saha Biswajit, Chakraborty Purushottam. Energy Procedia, 2013;41,80–109.

[5] Haag M, Gnaser H, Oechsner H. Fresenius J. Anal. Chem. 1995;353,565.

[6] Brison J, Muramoto S, Castner David G. J. Phys. Chem. C Nanomater Interfaces. 2010;114,5565–5573.

[7] Andersen CA, Hinthorne JR. Anal. Chem. 1973;45,142.

[8] Slodzian G. Phys. Scripta, 1983;T6,54.

[9] Williams P. Surf. Sci. 1979;90,588.

[10] Landau L. Physik. Z. Sowjetunion, 1932;2,46,46; Zener C. Proc. Roy. Soc., London, 1932;A137,696.

[11] Yu ML, Mann K. Phys. Rev. Lett. 1986;57,1476.

[12] Yu ML. in Sputtering by Particle Bombardment III (Eds. R. Behrisch and K. Wittmaack), Springer-Verlag, Berlin, 1991;91.

[13] van der Weg WF, Rol PK. Nucl. Instrum. Meth. 1965;38,274.

[14] Yu ML. in Proceedings of SIMS VI (Eds. A. Benninghoven et al) Wiley, NY, 1987;41.

[15] Canteri R, Moro L, Anderle M. in Proc. of SIMS VIII (Eds. A.Benninghoven, et al.), Wiley, NY, 1991;135.

[16] Wittmaack K. Surface Science, 1999;429,84.

[17] Schenkel T. in Ion Beam Analysis of Surfaces and Interfaces of Condensed Matter Systems (Ed. Chakraborty Purushottam), Nova Science, New York, 2002.

[18] Gao Y, Marie Y, Saldi F, Megion HN. Int. J. Mass Spectrom. Ion Proc. 1995;143,11.

[19] Gnaser H, Oechsner H. Surf. Sci. Lett. 1994;302,L289.

[20] Bloom S, Margenau H. Phys. Rev. 1985;85,670.

[21] Gnaser H, Oechsner H. Surf. Interface Anal. 1994;21,257.

[22] Saha Biswajit, Sarkar Subhendu, Chakraborty Purushottam, Gnaser Hubert. Surface Science, 2008;602,1061.

[23] Wilson RG, Stevie FA, Magee CW. SIMS - A Practical Handbook for Depth Profiling and Bulk Impurity Analysis, John Wiley and Sons, NY, 1989.

[24] Sarkar S, Chakraborty P, Gnaser H. Phys. Rev. B, 2004;70, 195427.

[25] Mootz T, Adriaens A, Adams F. Int. J. Mass Spectrom. Ion Process, 1996;156,1.

[26] Marie Y, Gao Y, Saldi F, Migeon H-N. Surf. Interface. Anal. 1995;23,38.

[27] Saha B, Chakraborty P. Nucl. Instrum. Methods Phys. Res. 2007;B258,218.

[28] Sarkar Subhendu, Datta Alokmay, Chakraborty Purushottam. J. Mater. Res. 2005;20,2639.

[29] Sarkar S, Chakraborty P, Sanyal MK, Caccavale F, Arora BM. Surf. Interface Anal. 2000;29,659.

[30] Warren BE. X-ray Diffraction. Addison Wesley: Reading, MA, 1969.

[31] Adachi S. J. Appl. Phys. 1982;53,8775.

[32] Hofmann S. Appl. Surf. Sci. 1993;70/71,9.

[33] Hofmann S. Surf. Interface Anal. 1994;21,673.

[34] Prudon G, Gautier B, Dupuy JC, Dubois C, Bonneau M, Delmas J, Vallard JP, Bremond G, Brenier R. Thin Solid Films 1997;294,54.

[35] Marseilhan D, Barnes JP, Fillot F, Hartmann JM, Holliger P. Appl. Surf. Sci. 2008;255,1412.

[36] Holliger P, Laugier F, Dupuy JC. Surf. Interface Anal. 2002;34, 472.

[37] Gavelle M, Scheid E, Cristiano F, Armand C, Hartmann JM, Campidelli Y, Halimaoui A, Fazzini PF, Marcelot O. J. Appl. Phys. 2007;102,074904.

[38] Saha Biswajit, Chakraborty Purushottam, Gnaser Hubert, Sharma Manjula, Sanyal Milan K. Appl. Phys. A, 2012;108, 671.

[39] Gnaser H. Surf. Sci. 1995;342,319.

[40] Gavelle M, Scheid E, Cristiano F, Armand C, Hartmann JM, Campidelli Y, Halimaoui A, Fazzini PF, Marcelot O. J. Appl. Phys. 2007;102,074904.

[41] Sharma M, Sanyal MK, Mukhopadhyay M, Bera M, Saha B, Chakraborty P. J. Appl. Phys. 2011;110,102204.

[42] Bayan Sayan, Chakraborty Purushottam. Applied Surface Science, 2014;303,233–240.

[43] Bayan Sayan, Mishra Sheo K, Satpati Biswarup, Srivastava Rajneesh K, Shukla Rajesh Kumar, Chakraborty Purushottam. J. Vac. Sci. Technol. B, 2016;34,061201–061208.

[44] Bayan Sayan, Satpati Biswarup, Chakraborty Purushottam. Surf. Interface Anal. 2014;47,37–44.

[45] Choudhury Biswajit, Bayan Sayan, Choudhury Amarjyoti, Chakraborty Purushottam. Journal of Colloid and Interface Science, 2016;465,1–10.

[46] Choudhury B, Borah B, Choudhury A. Photochem. Photobio. 88,257–264.

[47] Devi LG, Kavitha R. Appl. Catal. B: Environ. 2013;140,559–587.

[48] Bayan Sayan, Choudhury Biswajit, Satpati Biswarup, Chakraborty Purushottam, Choudhury Amarjyoti. J. Appl. Phys. 2015;117,095304.

[49] Shelby RA, Smith DR, Schultz S. Science, 2001;292,77.

[50] Hoffman Anthony J, Sridhar Aishwarya, Braun Phillip X, Alekseyev Leonid, Howard Scott S, Franz Kale J, Cheng Liwei, Choa Fow-Sen, Sivco Deborah L, Podolskiy Viktor A, Narimanov Evgenii E, Gmachl Claire. J. Appl. Phys. 2009;105, 122411.

Purushottam Chakraborty, a Former Senior Professor of Physics, Saha Institute of Nuclear Physics, Kolkata, India and a Former Adjunct Professor of Physics, University of Pretoria, South Africa is considered as one of the leading experts in Materials Science and Materials Analysis using Ion Beams. He was awarded the "**Most Eminent Mass Spectrometrist of India**" and conferred the "**Gold Medal**" by the Department of Atomic Energy (DAE), Government of India for his outstanding contributions in Secondary Ion Mass Spectrometry (**SIMS**). **He received "Premchand Roychand Scholarship (PRS)" and "Mouat Medal" of Calcutta University**.

His research areas include: Atomic Collisions in Solids, Ion-Beam Modifications and Analysis, Secondary Ion Mass Spectrometry (SIMS), Low-dimensional Materials, X-UV optics, Nonlinear Optics, Photonics, Plasmonics, etc.

He indigenously fabricated an RF-Quadrupole Mass Spectrometer for the first time in India for working on Atomic Collisions in Solids. **His "MCs_n^+ molecular-ion based SIMS" is considered to be innovative for compositional analysis of nanostructured materials.** His work on the **fabrication of 'layered Synthetic Microstructures (LSM)' is recognized as a pioneering contribution in the "Realization of Optical Devices for the Extreme Ultraviolet to Soft X-rays".** His works on "Metal-Glass Nanocomposites" have led to the remarkable achievements in the development of novel photonic materials.

He worked at FOM-Institute in Netherlands, ICTP and Padova University in Italy, Laval University in Canada, University of Pretoria in South Africa, Pontifical Catholic University of Rio de Janeiro in Brazil etc. **He delivered lectures** at Imperial College in **London**; *Maria Curie-Sk³odowska University and* Polish Academy of Sciences in **Poland**; Vanderbilt University, IBM T J Watson Research Centre, Rutgers University, Jackson State University, Furman University, Yale University in **USA**; Bielefeld University, Friedrich Schillar University, Kaiserslautern University in **Germany**; University of Western Australia, Newcastle University **Australia**; Osaka Electrocommunication University, Kyoto University, Spring-8, Nagoya Institute of Technology in **Japan**, National Taiwan University in **Taiwan**; Witwatersrand University, i-Themba Labs for Accelerator Sciences, Nelson Mandela University in **South Africa**; Asian Institute of Technology in **Thailand**, TIFR, IISc, IITs, Tezpur University, in **India**, etc.

He has delivered invited lectures at more than 140 international conferences across the globe and published more than 130 scientific papers including review articles, book chapters, etc.

He edited a book on "*Ion-beam Analysis of Surfaces and Interfaces of Condensed Matter Systems*" (**Nova Science Publishers**, New York, USA) and **Journal of Physics** – Conference Series **(UK)**. He is the Editor of "**Photonic Materials**", as a Section of the "**Encyclopedia of Materials: Electronics**" (To be published by **Elsevier Science**). He is editing as a Co-Editor of a book "*Nanomaterials for Sensing and Labelling Applications*" (**Springer**, Germany)

He is a **Fellow** of the **Indian Chemical Society** and **West Bengal Academy of Science and Technology.**